nature methods

Article

https://doi.org/10.1038/s41592-024-02575-1

Label-free nanoscopy of cell metabolism by ultrasensitive reweighted visible stimulated Raman scattering

Received: 12 June 2024

Accepted: 26 November 2024

Published online: 16 January 2025

Check for updates

Haonan Lin[1,2,3], Scott Seitz[4,5], Yuying Tan[2,3], Jean-Baptiste Lugagne[2,6], Le Wang[1,3], Guangrui Ding[1,3], Hongjian He[1,3], Tyler J. Rauwolf[7,8], Mary J. Dunlop[2,6], John H. Connor[4,5], John A. Porco Jr.[7,8], Lei Tian[1,2,3] & Ji-Xin Cheng[1,2,3,7]

Super-resolution imaging of cell metabolism is hindered by the incompatibility of small metabolites with fluorescent dyes and the limited resolution of imaging mass spectrometry. We present ultrasensitive reweighted visible stimulated Raman scattering (URV-SRS), a label-free vibrational imaging technique for multiplexed nanoscopy of intracellular metabolites. We developed a visible SRS microscope with extensive pulse chirping to improve the detection limit to ~4,000 molecules and introduced a self-supervised multi-agent denoiser to suppress non-independent noise in SRS by over 7.2 dB, resulting in a 50-fold sensitivity enhancement over near-infrared SRS. Leveraging the enhanced sensitivity, we employed Fourier reweighting to amplify sub-100-nm spatial frequencies that were previously overwhelmed by noise. Validated by Fourier ring correlation, we achieved a lateral resolution of 86 nm in cell imaging. We visualized the reprogramming of metabolic nanostructures associated with virus replication in host cells and subcellular fatty acid synthesis in engineered bacteria, demonstrating its capability towards nanoscopic spatial metabolomics.

Imaging live cells and intact tissues at the nanoscopic level can provide insights into how intracellular nanostructures assemble and interact, fostering advances in molecular biology and precision medicine[1]. By adding functional covalent tags, far-field fluorescence nanoscopy[2–5] has achieved cellular organelle imaging at the resolution of tens of nanometers. However, imaging nutrients and metabolites at comparable resolutions remains a notable challenge. For small metabolites, fluorescence imaging is challenging because the labels perturb their functions. Imaging mass spectrometry[6–8] provides comprehensive metabolic profiles but suffers from poor spatial resolution and low throughput. These limitations collectively prohibit a deep understanding of the intracellular nanostructures from a spatial metabolomics[9,10] perspective.

Vibrational spectroscopy techniques, including Raman scattering and infrared absorption, can image intracellular metabolites by detecting their intrinsic chemical bond vibrations. Advanced vibrational spectroscopic imaging techniques, such as coherent anti-Stokes Raman scattering (CARS)[11], SRS[12] and mid-infrared photothermal (MIP)[13]

[1]Department of Electrical and Computer Engineering, Boston University, Boston, MA, USA. [2]Department of Biomedical Engineering, Boston University, Boston, MA, USA. [3]Photonics Center, Boston University, Boston, MA, USA. [4]Department of Virology, Immunology, and Microbiology, Boston University Chobanian & Avedisian School of Medicine, Boston, MA, USA. [5]National Emerging Infectious Diseases Laboratories, Boston University Chobanian & Avedisian School of Medicine, Boston, MA, USA. [6]Biological Design Center, Boston University, Boston, MA, USA. [7]Department of Chemistry, Boston University, Boston, MA, USA. [8]Center for Molecular Discovery (BU-CMD), Boston University, Boston, MA, USA. e-mail: jxcheng@bu.edu

microscopy, have been developed for high-speed label-free bioimaging at resolutions of ~300 nm. Numerous efforts have improved the spatial resolution of vibrational imaging. Harnessing non-linear responses from saturation[14–17], higher order susceptibility[18] and temporal harmonics[19], resolution enhancements of up to twofold have been achieved. Structured-illumination SRS[20,21] and CARS[22] have been reported to achieve ~1.4-fold resolution enhancement. Through sample expansion, SRS can resolve features that are closely packed in the original sample to reach effective resolutions below 100 nm[23,24]. Deconvolution SRS has been applied to super-resolve sparse and concentrated dot structures, such as small lipid droplets[25]. Shifting excitation from near-infrared to visible wavelengths has pushed the lateral resolution of SRS to 130 nm[26]. Furthermore, stimulated Raman excited fluorescence[27] has triggered the adaptation of fluorescence nanoscopy techniques, including stimulated emission depletion[28] and reversible saturable optical fluorescence transitions[29,30], to improve SRS resolution to ~ 90–150 nm.

Despite the burgeoning development of super-resolution vibrational imaging methodologies, sensitivity—one of the most critical aspects of practical vibrational nanoscopy—has been overlooked. Unlike fluorescence with single-molecule sensitivity, the detection limit of near-infrared SRS is at the millimolar level. This limitation becomes particularly pronounced when resolving structures smaller than the laser focal volume, where the amount of excited molecules is markedly reduced. Therefore, super-resolution vibrational imaging techniques that lack sensitivity fall short in detecting metabolic nanostructures. Approaches based on saturation and higher-order processes suffer from reduced sensitivity owing to smaller cross-sections. Structured illumination faces sensitivity limitations owing to its lower photon density than that of laser scanning methods. Sample expansion techniques dilute molecular concentrations in organelles, which diminishes sensitivity. Although deconvolution does not affect sensitivity, it requires a high signal-to-noise ratio (SNR) because of its susceptibility to noise. Visible SRS benefits from the cross-section enhancement but faces limitations in sensitivity due to photodamage from visible ultrafast lasers and strong non-Raman backgrounds. Although super-resolution SRS using fluorescence reporters provides sufficient sensitivity, using fluorescence tags leads to compatibility issues for small metabolites. Thus a notable gap persists for non-fluorescent methods that provide sufficient sensitivity and specificity for multiplexed imaging of metabolites at sub-100-nm resolutions.

Here, we introduce URV-SRS, a label-free vibrational nanoscopy modality for resolving metabolic nanostructures with high sensitivity and specificity. The sensitivity enhancement is synergistically achieved through instrumentation-based signal enhancement and computation-based noise suppression. To enhance the signal level, we developed a spectral-focusing visible SRS setup with extensive pulse chirping of 4 picoseconds, which substantially reduced phototoxicity owing to lower peak power and suppressed non-Raman backgrounds owing to temporal dispersion. Under biocompatible power settings, our setup achieved a 20-fold sensitivity enhancement over near-infrared (NIR) SRS. To suppress noise, we developed Noisy-As-Clean with consensus equilibrium (NACE), a self-supervised denoising algorithm capable of removing non-independent noise in SRS. This is achieved by generating experimental noisier–noisy image pairs, taking them as input–output to train a series of deep-learning denoisers at different SNR levels, and integrating all networks through multi-agent consensus equilibrium[31] for SNR-matched denoising of the noisy image. Consequently, NACE has increased the SNR by more than 7.2 dB in biological samples. Together, these improvements have boosted the detection sensitivity by a factor of ~50 compared with that of current NIR SRS.

The enhanced sensitivity has subsequently offered opportunities to enhance the spatial resolution of visible SRS to nanoscopic levels. As a two-photon, non-linear process, the optical transfer function (OTF) of visible SRS is the convolution between the pump and Stokes OTFs, which extends the spatial frequency support to the sub-100-nm range. However, it suffers from rapid attenuation at higher spatial frequencies, making it susceptible to noise contamination and therefore cannot be effectively utilized at low SNR conditions. To fully leverage the spatial frequency support, we introduced Fourier reweighting[32,33] after NACE denoising (FURNACE), which reshapes the SRS OTF in the denoised image to robustly amplify the high spatial frequencies previously overwhelmed by noise. Rigorously validated by Fourier ring correlation (FRC)[34], URV-SRS has reached a lateral resolution of 86 nm and an axial resolution of 400 nm in cell imaging. To demonstrate the potential of URV-SRS for nanoscopic metabolic imaging, we explored two applications in molecular virology and synthetic biology. These include high-content, three-dimensional (3D) imaging of virus-induced reprogramming of metabolic nanostructure in host cells, as well as compositional imaging of fatty-acid synthesis in individual engineered bacteria. The results showcase the potential of URV-SRS towards nanoscopic spatial metabolomics across a wide spectrum of biological systems.

Results

Highly sensitive visible SRS through extensive chirping

The lab-built visible SRS setup is illustrated in Fig. 1a. Two broadband femtosecond visible lasers at 453 nm and 523 nm were produced to target the carbon-hydrogen (CH) region. Details of the optical and electronic components are included in the Methods. Owing to the short-wavelength and near-resonance enhancement, the Raman cross-section under visible excitation is at least 23 times greater than that of its NIR[26] counterparts (Supplementary Note 1). However, ultrafast visible lasers with high peak powers can induce severe non-linear photodamage and strong parasitic non-Raman pump-probe background, leading to a lower biocompatible power limit and a poor signal-to-background ratio. These two bottlenecks hinder visible SRS from achieving the increase in sensitivity expected from the larger cross-section.

Here, we demonstrate that extensive chirping of femtosecond pulses offers an elegant solution to simultaneously address the two bottlenecks in visible SRS. As depicted in the inset of Fig. 1a, both the pump and Stokes beams were linearly chirped by glass rods, extending the pulse duration from femtoseconds to a few picoseconds and temporally dispersing frequency components. This substantially reduces the peak intensity as the pulse extends temporally, thereby reducing non-linear photodamage. By combining this technique with high-speed scanning to alleviate cumulative photothermal effects, we significantly increased the photodamage threshold. A series of experiments (Fig. 1b, Extended Data Fig. 1 and Supplementary Note 2) was performed to determine the photodamage limits on multiple cell types. By chirping the pulse from 0.15 ps to 4 ps, a tenfold increase in the power limit was achieved. Meanwhile, we quantified the change of SRS signal intensity under different pulse-chirping conditions. At the same average powers, chirping from 0.15 ps to 4 ps led to a 2.5-fold decrease in SRS signal (Extended Data Fig. 2a,b and Supplementary Note 3). Considering the tenfold gain in the biosafety power limit, the 4-ps condition results in an overall increase in the SRS signal intensity for cell imaging.

Furthermore, extensive chirping effectively suppresses the parasitic non-Raman pump–probe background. As depicted in Extended Data Fig. 2c,d, we imaged SJSA-1 bone cancer cells under the 2.5-ps and 4-ps conditions to examine the off-resonance signals. At comparable on-resonance signal levels, the off-resonance signal decreased by approximately five times (Extended Data Fig. 2e). This can be explained by the difference in excitation bandwidth between Raman and competing processes. Owning to linearly matched chirping, we achieved a high spectral resolution of 8.2 cm^{-1} in the CH region (Supplementary Fig. 1 and Supplementary Note 4). Because all the competing background processes disperse the signal across the entire spectral bandwidth

https://doi.org/10.1038/s41592-024-02575-1

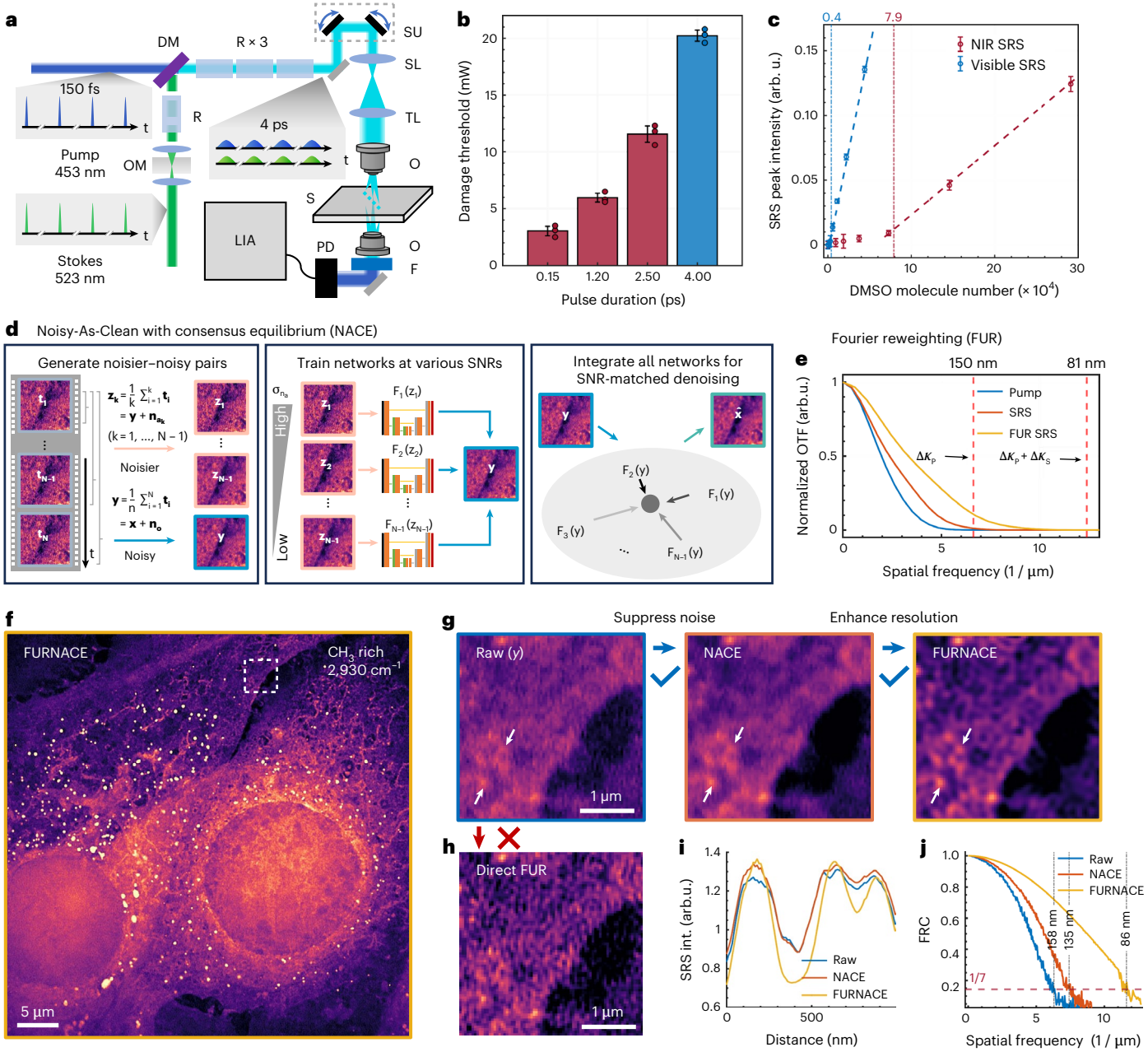

Fig. 1 | Principle of label-free metabolic nanoscopy by URV-SRS. a, Optical setup. DM, dichroic mirror; OM, optical modulator; R, rod; SU, scanning unit; SL, scan lens; TL, tube lens; O, objective; S, stage; F, filter; PD, photodiode; LIA, lock-in amplifier. **b**, Cell photodamage threshold power under different pulse durations. Error bars were derived from biological replicates of different cell types ($n = 3$). **c**, Limit of detection of dimethyl sulfoxide (DMSO) in terms of molecule number within the laser excitation volume for visible and NIR SRS. Sloped dashed lines represent the linear fitting between the SRS peak intensity and molecule number. Vertical dashed lines show the molecule number at the baseline intensity + 3σ levels; the baseline intensities are mean values at zero concentrations, and σ are the noise levels measured as the s.d. in a background area ($n = 400$ pixels). arb.u., arbitrary units. **d**, Workflow of self-supervised denoising through NACE, including generating multiple noisier-noisy (z_k–y) image pairs, training individual U-Net denoisers at different SNRs, and integrating all networks for SNR-matched denoising of noisy image (y) through consensus equilibrium. **e**, Optical transfer function (OTF) for the pump, SRS and Fourier reweighted (FUR) SRS. Cut-off spatial frequencies for the pump, Stokes and SRS are Δkp, $\Delta\kappa_S$ and $\Delta\kappa_p$+$\Delta\kappa_S$. Values for $\Delta\kappa_p$ and $\Delta\kappa_p$+$\Delta\kappa_S$ are shown in dashed lines. **f**, Visible SRS imaging of SKOV3 ovarian cancer cells at 2,930 cm^{-1} through FUR after NACE (FURNACE). Three independent experiments were repeated with similar results. **g**, Zoom-in of the dashed box region in **f**, showing the raw image (y), NACE denoising output and FURNACE resolution enhancement output. **h**, Direct application of FUR to the raw image (y). **i**, Line profiles between the two arrows in **g**. **j**, Single-image FRC analysis for the raw, NACE and FURNACE. The horizontal dashed line indicates the 1/7 resolution criteria; vertical dashed lines represent the corresponding lateral resolutions.

(~400 cm^{-1}) whereas Raman exhibits a narrow instantaneous excitation bandwidth (8.2 cm^{-1}), the signal-to-background ratio at Raman on-resonance was significantly improved.

We evaluated the limit of detection (LOD) for visible SRS and NIR SRS at their respective biocompatible power limits. We measured the serial dilution of DMSO and obtained LODs of ~6 mM for NIR SRS and ~2 mM for visible SRS (Extended Data Fig. 3). Notably, the baseline in visible SRS is reduced to 1/6 of its NIR counterpart, owing to extensive chirping. Quantifying the LOD on the basis of molar concentration could overestimate the performance in sensing nanostructures that are smaller than the laser focal volume. Therefore, we derived the LOD in terms of absolute molecule number by accounting for the excitation

volumes. We benchmarked the excitation volume of visible SRS to be approximately six times smaller than its NIR counterpart (Extended Data Fig. 4a–c and Supplementary Note 5). Together with a threefold enhancement of LOD in molar concentration, the LOD of visible SRS has reached 0.4×10^4 in absolute DMSO molecule number, achieving a 20-fold enhancement over NIR SRS, which has an LOD of 7.9×10^4 (Fig. 1c and Extended Data Fig. 4d).

Self-supervised non-independent noise removal through NACE

To synergize our method with instrumentation-based signal enhancement, we developed a noise-suppression algorithm to enhance sensitivity. Because it is challenging to obtain higher SNR ground truth at the sensitivity limits, a self-supervised or unsupervised method capable of denoising from single noisy images is required. Traditional internal statistical methods, such as Block-Matching and 3D filtering (BM3D)[35] and Noise2Void (N2V)[36], rely on the prior knowledge of noise following independent and identical distributions. However this condition is not fulfilled in SRS microscopy, or broadly, modalities relying on lock-in detection (Supplementary Note 6 and Supplementary Fig. 2). We observed noise correlations between adjacent pixels along the fast laser scanning axes, regardless of the lock-in detection configuration (Supplementary Fig. 3).

Supervised training, in which the noise statistics and image priors are learned directly from noisy–clean image pairs, remains the most robust approach for eliminating sophisticated, non-independent noise. Under the condition of having no higher-SNR ground truth for training, it has proven possible to train a network with noisier–noisy image pairs, in which the noisier image is generated by adding additional noise identical to the observed noise. The trained network can then effectively remove the observed noise in the noisy target image[37]. Our 'fast-scanning + multiple averaging' strategy, originally designed to minimize photodamage, provides an elegant way to introduce additional experimental noise sharing the same sophisticated noise statistics with the observed noise. As illustrated in Fig. 1d, we reduced the number of averaged frames in a fast-scanning sequence $[\mathbf{t_1}, \mathbf{t_2}, \ldots, \mathbf{t_N}]$ to generate a series of noisier images ($\mathbf{z_k}$) with SNR lower than the whole-sequence averaged raw image ($\mathbf{y}$) with observed noise ($\mathbf{n_o}$). This is equivalent to introducing additional noise ($\mathbf{n_{ak}}$) to $\mathbf{y}$ with various noise levels ($\sigma_{n_{ak}}$) (Extended Data Fig. 5a).

In the next step, each noisier–noisy image pair ($\mathbf{z_k}$–$\mathbf{y}$) was used to train a U-Net[38] at the noise level of $\sigma_{n_{ak}}$. Our noisier image-generation strategy does not guarantee SNR matching between the additional noise and the observed noise (that is, $\sigma_{n_{ak}} \neq \sigma_{n_o}$). As shown in Extended Data Fig. 5b, using SNR-mismatched individual networks to denoise $\mathbf{y}$ has led to either insufficient noise removal ($\sigma_{n_{ak}} < \sigma_{n_o}$) or over-smoothing ($\sigma_{n_{ak}} > \sigma_{n_o}$). To address this challenge, we combined all SNR-mismatched denoisers, for ensemble denoising with SNR-matching performance. This was achieved under the consensus equilibrium (CE)[31] framework, which treated each individual U-Net denoiser as an image prior (that is, regularization) and combined them into a single inverse problem in an optimization-free manner. By balancing the weights of the contribution from each U-Net denoiser on the basis of the difference between $\sigma_{n_{ak}}$ and σ_{n_o}, CE adaptively generated denoising results, having comparable performance to SNR-matched denoising. Consequently, the NACE method improved the SNR of the raw image by 2.3 times (7.2 dB) without introducing over-smoothing or artifacts. Details on the algorithm and implementation are included in the Methods and Supplementary Note 7.

We benchmarked the performance between NACE and other self-supervised denoisers, including BM3D and N2V (Supplementary Fig. 4). Owing to correlated noise and sophisticated object structures of the visible SRS dataset, BM3D and N2V produced either strip or checkerboard artifacts. In comparison, none of the artifacts were observed in NACE owing to its unique learning strategy. Quantitatively, we benchmarked the performance of NACE using a NIR SRS dataset of SKOV3 cells with high-SNR baseline images (Extended Data Fig. 6a,b and Supplementary Note 8). Denoising results by NACE, BM3D and N2V were shown in Extended Data Fig. 6c. Structural similarity index (SSIM)[39] and peak signal-to-noise ratio (PSNR) values were shown in Extended Data Fig. 6d. Both the denoised results and quantification metrics suggest that NACE outperformed traditional BM3D and self-supervised N2V denoisers in removing non-independent noise.

Robust resolution enhancement through FURNACE

In SRS microscopy, because the signal is measured at the same frequencies as the excitation fields, the phase-matching condition is automatically matched[40]. This property eliminates the coherent imaging artifacts and enables the use of intensity point spread function (PSF) for image formation. The linear dependency between the signal and the object function further simplifies image interpretation, allowing for linear deconvolution or spatial frequency reweighting used in fluorescence microscopy. The intensity PSF of SRS is defined by the multiplication of two co-localized, diffraction-limited pump and Stokes PSFs (Supplementary Fig. 5). The resulting SRS optical transfer function (OTF) is the convolution of the pump and Stokes OTFs, which has a frequency support as the sum of the pump and Stokes passbands ($\Delta\kappa_{SRS} = \Delta\kappa_p + \Delta\kappa_S$), allowing for spatial frequencies up to 81 nm (Fig. 1e). Despite this extension, the convolution process leads to rapid attenuation of the SRS OTF magnitude at higher spatial frequencies, resulting in a practical enhancement of spatial resolution that is less than the frequency support extension. To fully leverage the spatial frequency support of SRS, we implemented a Fourier reweighting[32,33] (FUR) function to remodel the SRS OTF into the scaled version of a normal circular pupil OTF (Methods). This adjustment amplifies the higher spatial frequencies, effectively improving the lateral resolution from 125 nm to 83 nm, as evidenced in Supplementary Fig. 6. Nonetheless, SNR is crucial for effective application of FUR in biological samples. Under low-SNR conditions, minute spatial frequencies are easily overwhelmed by noise, and direct reweighting will introduce high-spatial-frequency ringing artifacts.

To achieve robust resolution enhancement in biological systems, we implement FUR after NACE denoising (FURNACE). This tandem algorithm first employs NACE to suppress sophisticated noise, followed by FUR to amplify high spatial frequencies. As shown in Fig. 1f, we imaged SKOV3 ovarian cancer cells using the developed visible SRS setup and applied the FURNACE algorithm. A zoom-in examination at the dashed region in Fig. 1f is provided in Fig. 1g, illustrating the stepwise improvements from denoising (through NACE) to resolution enhancement (through FUR). To demonstrate how NACE enables robust spatial frequency amplification, we directly applied reweighting to the raw image. This comparison highlighted the introduction of severe ringing artifacts (Fig. 1h) owing to the amplification of noise. Figure 1i compares line profiles across specified arrows in Fig. 1g for the Raw, NACE and FURNACE-processed images, showing robust resolution improvement with FURNACE.

Additionally, we used single-frame FRC[34] to quantitatively measure spatial resolution (Methods). Because FRC is dependent on both SNR and OTF, it effectively captures the impact of denoising and reweighting on resolution. Further, accounting for the entire field of view (FOV) avoids overestimating resolution on the basis of the widths of specific high-SNR structures. As illustrated in Fig. 1j, FRC curves for Raw, NACE and FURNACE images revealed spatial resolutions of 158 nm, 135 nm and 86 nm, respectively, according to the 1/7 criterion. To confirm that FURNACE can robustly enhance the spatial resolution without introducing notable artifacts, we performed two validation experiments using SRS datasets with ground-truth spatial structures, including synthetic handwriting digits (Supplementary Note 9 and Supplementary Fig. 7) and cell images (Supplementary Note 10 and Supplementary Fig. 8).

URV-SRS nanoscopy of virus-replication metabolism

Understanding how viruses hijack metabolic resources is crucial for developing antiviral strategies to impede their replication. Viruses establish central replication sites within host cells, where they synthesize new viral progeny[41]. However, how metabolites are recruited to these sites and spatially organized to facilitate virion production remains poorly investigated, owing to the lack of methods to perform high-content metabolic imaging in intracellular nanostructures. This observational gap hinders a complete understanding of viral hijacking of cellular processes and restricts identifying effective strategies to disrupt metabolic resource reallocation and viral replication.

In this study, we used URV-SRS to bridge the knowledge gap in virus–host interactions. We imaged both control (mock-infected) and Zika virus (ZIKV) infected VERO cells at 2,930 cm^{-1} and 2,850 cm^{-1} to highlight CH_3 and CH_2 bonds. In the control group, we identified organelles such as lipid droplets, mitochondria, vesicles, nuclear membrane and endoplasmic reticulum tubules (dashed box 1 in Fig. 2a,b), on the basis of morphological and vibrational signatures. Inside the nucleus, we observed nucleoli (2–5 µm in diameter) with stronger signals than in the surrounding nucleoplasm environment. For ZIKV-infected cells, substantial changes in cellular morphology and chemical composition were observed (Fig. 2c–i). Notably, the infection altered the nucleoplasm environment. Nucleoli were not identified in the infected cells, whereas highly aggregated CH_3-rich domains were observed inside the nucleus (dashed boxes 2 and 3 in Fig. 2c,d,f), indicative of concentrated proteins and nucleic acids. Line profiles across intranuclear hotspots revealed ~200-nm separated peaks, suggesting that these structures may be condensed chromatin domains (CDs)[42], potentially formed through interactions with ZIKV NS5, the viral RNA polymerase known to bind chromatin DNA and alter host gene transcription[43] (Fig. 2e,g).

In the ZIKV-infected cells, we noted substantial reorganization of the endoplasmic reticulum (ER), with enhanced metabolic signals in both CH_3 and CH_2 channels, indicative of virus-replication sites (dashed box 4 in Fig. 2c). As suggested by previous electron microscopy studies[41], the replication sites are densely packed ER tubules that twist and branch to form sponge-like network structures. Closer inspection (Fig. 2h) revealed heterogeneous nanostructures in these sites, containing densely convoluted membranes and multiple lipid-rich hotspots (for example, S1 and S2) that likely represent interconnected double-membrane vesicles. Additionally, areas like S3 showed pronounced CH_3 signals. We quantified metabolic changes between the ER and replication sites by leveraging the linear relationship between SRS intensity and molecular concentration (Images of all replication sites are included in Supplementary Fig. 9). Data in Fig. 2j show that, in the virus-infected cells, SRS signals within the replication sites exhibit approximately twofold stronger signals than the surrounding ER at both 2,930 cm^{-1} and 2,850 cm^{-1}. The intensity difference is due to the condensation of the ER tubules in the replication sites, which increased the local concentrations of the metabolites. When comparing the ERs in the two groups, only a significant decrease in at 2,930 cm^{-1} was observed. This indicates that replication sites actively recruit lipids and metabolites from diverse sources, rather than merely concentrating existing ER components.

To verify that the observed morphological and metabolic alterations were due to ZIKV infection, we added synthetic (±)-eucalyprobusone G (CMLD013697), a Zika antiviral (RdRp) inhibitor, and two related synthetic compounds, eucalyprobusone A (CMLD013694) and DFPG dimer (CMLD013695), to the infected cells and analyzed their morphological and metabolic responses. Details of the chemical synthesis are provided in the Supplementary Information. We used SRS at 2,930 cm^{-1} to examine the ZIKV-infected cells with antiviral compound treatment, mock-infected control cells and the ZIKV-infected cells (Extended Data Fig. 7a). We noticed that, in all the groups treated with the antiviral compound, fewer cells showed structural remodeling induced by virus infection, including the aggregated replication sites and the intranuclear domain structures. To further confirm the observation, we counted the number of abnormal cells with structural remodeling and normal cells and observed a notable reduction of the percentage of the abnormal cells in the treated groups (Extended Data Fig. 7b).

To benchmark the performance of URV-SRS, we used NIR SRS to image ZIKV-infected cells with virus-replication sites (Extended Data Fig. 8). Owning to the limited lateral resolution of ~300 nm, NIR SRS was insufficient to reveal membrane structures within the replication site (Extended Data Fig. 8c). In comparison, the raw visible SRS image and the FURNACE output (including denoising and reweighting) were shown in Extended Data Fig. 8d,e, demonstrating the higher raw resolution of visible SRS and the FURNACE resolution enhancement that jointly contributed to the observation of the complex membrane structures within the replication sites.

High-content metabolic profiling through hyperspectral imaging

To comprehensively understand metabolic reprogramming related to the extensive structural rearrangements after ZIKV infection, we performed hyperspectral visible SRS imaging of the same cells depicted in Fig. 2. Using pixel-wise LASSO unmixing[44] (Supplementary Fig. 10 and Methods), we generated high-content metabolic maps of major biomolecules, including protein, fatty acid, cholesterol, carbohydrate and nucleic acid, using standard references (Fig. 3b). These maps show spatially distinct intracellular organizations of the metabolites. In the control group, we observed protein in both the cytoplasm and nucleoplasm. As major intracellular lipid species, fatty acid and cholesterol showed high concentrations inside ER and LDs. Most carbohydrates were located in the ER, aligning with previous research on their distribution in mammalian cells[44]. Nucleic acid, representing both intracellular DNA and RNA, was observed in the nucleoplasm and ER. Figure 3c depicts the zoom-in view of the same cell region shown in Fig. 2d, further confirming the metabolic basis of the identified organelles and structures.

In the ZIKV-infected cells, we identified that the nucleoplasm's aggregated domain structures (Fig. 3d) were rich in protein, nucleic acid and carbohydrate (deoxyribose), which provided further evidence confirming that the structures were chromatin domains. Additionally, we detected cholesterol enrichment in these aggregates, which has been reported to exist in nucleus microdomains linked with gene transcription[45]. Zooming into ZIKV replication sites (Fig. 3e) revealed all major metabolites congregating to support virus replication, with CH_2-rich areas S1 and S2 showcasing high fatty acid and cholesterol levels, indicative of double-membrane vesicles. The CH_3-rich structure S3, enriched in protein, nucleic acid and carbohydrate, likely represents convoluted membranes for virus synthesis.

Statistical analysis of high-content metabolic profiles (Fig. 3f) in both mock and infected cells' ER and replication sites confirmed that there were significantly higher molecular concentrations at replication sites than in normal ER, attributed to increased levels of all major metabolites—fatty acid and cholesterol by ~3 times, and protein, carbohydrate and nucleic acid by ~1.5 times; conversely, the ER in ZIKV cells showed a decrease in total metabolic content, mainly owing to a ~2-fold reduction in protein and nucleic acid, whereas fatty acid, cholesterol and carbohydrate levels remained relatively constant. This aligns with prior quantifications (Fig. 2c) and offers further insights towards uncovering the metabolic reprogramming and biomarkers of ZIKV infection.

Extending URV-SRS nanoscopy to 3D

Using URV-SRS, we have achieved label-free, high-content metabolic nanoscopy to explore intracellular structures and organelles. However, given the heterogeneity of these structures, 3D imaging is essential for a complete understanding of their spatial organization. As a two-photon process involving two tightly focused visible lasers, URV-SRS offers

https://doi.org/10.1038/s41592-024-02575-1

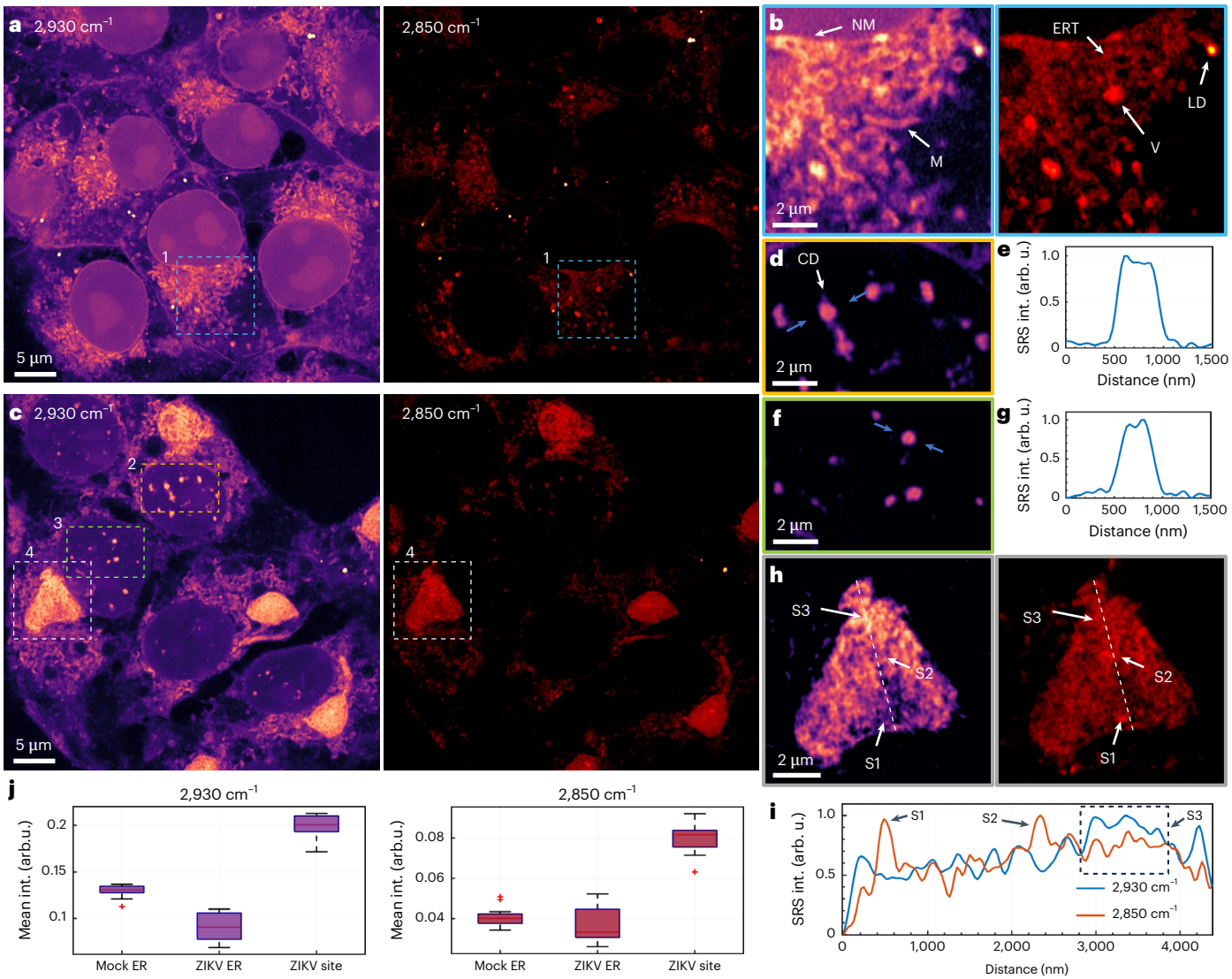

Fig. 2 | URV-SRS imaging of virus replication metabolism. a, URV-SRS imaging of control (mock-infected) VERO cells at 2,930 cm^{-1} and 2,850 cm^{-1}. Four independent experiments were repeated with similar results. **b**, Zoom-in of the dashed box 1 in **a** at both 2,930 cm^{-1} and 2,850 cm^{-1}. NM, nuclear membrane; M, mitochondria; ERT, endoplasmic reticulum tubules; LD, lipid droplets; V, vesicles. **c**, URV-SRS imaging of ZIKV-infected VERO cells at 2.930 cm^{-1} and 2,850 cm^{-1}. Four independent experiments were repeated with similar results. **d**, Zoom-in of the dashed box 2 in **c** at 2,930 cm^{-1}. CD, chromatin domain. **e**, Line profile between the two arrows in **d**. **f**, Zoom-in of the dashed box 3 in **c** at 2,930 cm^{-1}. **g**, Line profile between the two arrows in **f**. **h**, Zoom-in of the dashed box 4 in **c** at both 2,930 cm^{-1} and 2,850 cm^{-1}. S1, S2 and S3 represent 3 spots highlighted by the arrows along the dotted line. **i**, Line profiles along the dashed lines in both channels in **h**. Positions of S1, S2 and S3 in **h** are highlighted by arrows. **j**, Quantification of metabolic concentrations of CH_3 at 2,930 cm^{-1} and CH_2 at 2,850 cm^{-1} in the mock ER, ZIKV ER and ZIKV replication sites. $n = 14$ for the mock group and 9 for the ZIKV group. The boxes show the interquartile range (IQR), the red lines indicate medians, the black lines extend to 1.5 times the IQR and the red data points are the outliers.

excellent axial sectioning capability. As demonstrated in Fig. 4a, we achieved an axial resolution of 405 nm, aligning with the theoretical axial resolution that was calculated in Supplementary Note 3.

Empowered by sub-100-nm lateral and 400-nm axial resolutions, we performed 3D URV-SRS imaging on ZIKV-infected cells to map the entire nanoscopic structural framework. Supplementary Video 1 shows a volumetric stack spanning 3.5 μm (z = 18.5–21.9 μm) with a step size of 200 nm, covering the full volume of the cells. Figure 4b presents an image at a depth of 19.3 μm, along with a maximum projection and a color-coded axial projection, providing the 3D morphology of nanoscopic structures within ZIKV-infected cells. To verify the enhancement of FURNACE, we compared the zoom-in maximum projection of a replication site (dashed box 5 in Fig. 4b) from Raw, NACE and FURNACE (Fig. 4c,d). The FURNACE output shows detailed membrane layer structures invisible in the raw data.

3D nanoscopic imaging provided additional insights into cell nanostructures related to virus replication. Figure 4e highlights a replication site's upper layer (20.5–21.9 μm), marked by the dashed box 1 in Fig. 4b, which tightly encircles the cell nucleus. Figure 4f zooms into the ER region (dashed box 2 in Fig. 4b), displaying the clearly visible 3D membrane structures. As depicted in Fig. 4g, the zoom-in of the dashed box 3 in Fig. 4b shows a complex 3D network in the cell nucleus, connecting the aggregated domains identified in the two-dimensional (2D) images. In Fig. 4h, we mapped the 3D structures of a replication site (dashed box 4 in Fig. 4b), depicting cage-like structures upheld by highly convoluted membranes interspersed with vesicles. As suggested by Supplementary Video 1, owning to the highly heterogeneous 3D cell structure and the high axial resolution, nucleoli were visible in the depth range of 18.9–19.9 μm but were not found in other layers. This confirms the presence of nucleoli in the virus-infected cells and explains the absence of nucleoli in Fig. 2c.

https://doi.org/10.1038/s41592-024-02575-1

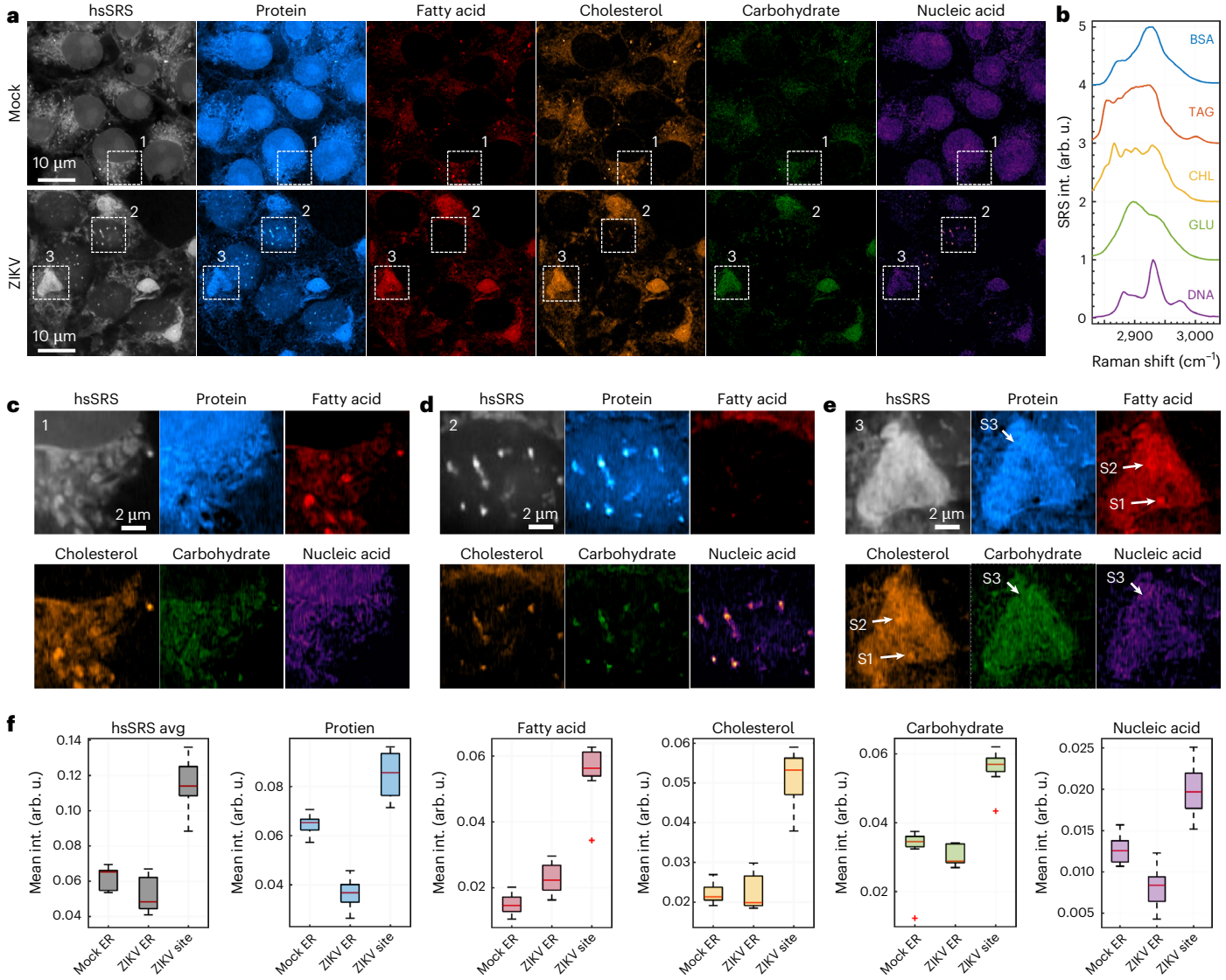

Fig. 3 | High-content metabolic imaging through hyperspectral URV-SRS and spectral unmixing. a, Raw hyperspectral visible SRS (hsSRS, spectral sum shown) of mock and ZIKV cells in the same FOV as in Fig. 2, followed by five-component high-content metabolic mapping of protein, fatty acid, cholesterol, carbohydrate and nucleic acid. Four independent experiments were repeated with similar results. Dashed boxes with labels 1, 2 and 3 are highlighted in all channels. **b**, SRS reference spectra of the target metabolites for spectral unmixing. Protein, fatty acid, cholesterol, carbohydrate and nucleic acid are represented by bovine serum albumin (BSA), triglyceride (TAG), cholesterol (CHL) powder, glucose (GLU) and cell-extracted deoxyribonucleic acid (DNA), respectively. **c**, Zoom-in of the dashed box 1 in **a**, indicating the ER regions in a mock-infected cell. **d**, Zoom-in of the dashed box 2 in **a**, highlighting the intranuclear aggregated domains. **e**, Zoom-in of the dashed box 3 in **a**, showing the virus-replication site. Each zoom-in contains the raw hyperspectral SRS (spectral sum) and five-component metabolic maps. **f**, Quantification of the overall metabolic content (hsSRS average), and levels of individual metabolic species in the mock ER, ZIKV ER and ZIKV replication sites. $n = 14$ for the mock group and 9 for the ZIKV group. The boxes show the IQR, the red lines indicate medians, the black lines extend to 1.5 times the IQR and the red data points are the outliers.

URV-SRS nanoscopy of chemical synthesis in single bacteria

Escherichia coli can be genetically engineered to produce high-demand fatty acids as bioproducts[46], offering a sustainable alternative to petroleum-based synthesis. However, low yield is a major bottleneck in scaling bio-production to an industrial level. Single-cell production heterogeneity has been shown to play an important role in limiting the yield[47]. The underlying bacterial mechanisms driving this cell-to-cell variation are not well understood, largely owing to the absence of techniques for in vivo quantitative metabolic imaging at the nanoscale, which is necessary to observe the minute intra-bacterial structures involved in these processes. This gap hinders advancements in strategies aimed at reducing the impact of heterogeneity on the production yield.

Here, we used URV-SRS to study nanoscopic metabolic profiles in a biofuel-producing strain (AbTE*-FV50)[48]. Figure 5a presents two-color URV-SRS imaging at CH_3-rich 2,930 cm^{-1} and CH_2-rich 2,850 cm^{-1}. Figure 5b shows a zoom-in of cells with active fatty acid production (dashed box in Fig. 5a), with line profiles along the dotted lines shown in Fig. 5c. Notably, at location S1 in the panel, we resolved membranes and cell walls that were not detected by NIR SRS imaging of the same strain[48] (Supplementary Fig. 11). This clarity results from the enhanced lateral and, crucially, axial resolution that is finer than the bacteria's diameter, allowing for subcellular sectioning. Further, we pinpointed sites (S2) at which fatty acids were transferred from the cell to the environment, marked by stronger SRS signals at 2,850 cm^{-1} owing to elevated concentrations of fatty acids. Membranes near these sites displayed heightened signals, forming domain hotspots (the dashed circle), likely as a cellular response to the stress from fatty acid toxicity[49]. Investigating these phenomena further could elucidate whether

https://doi.org/10.1038/s41592-024-02575-1

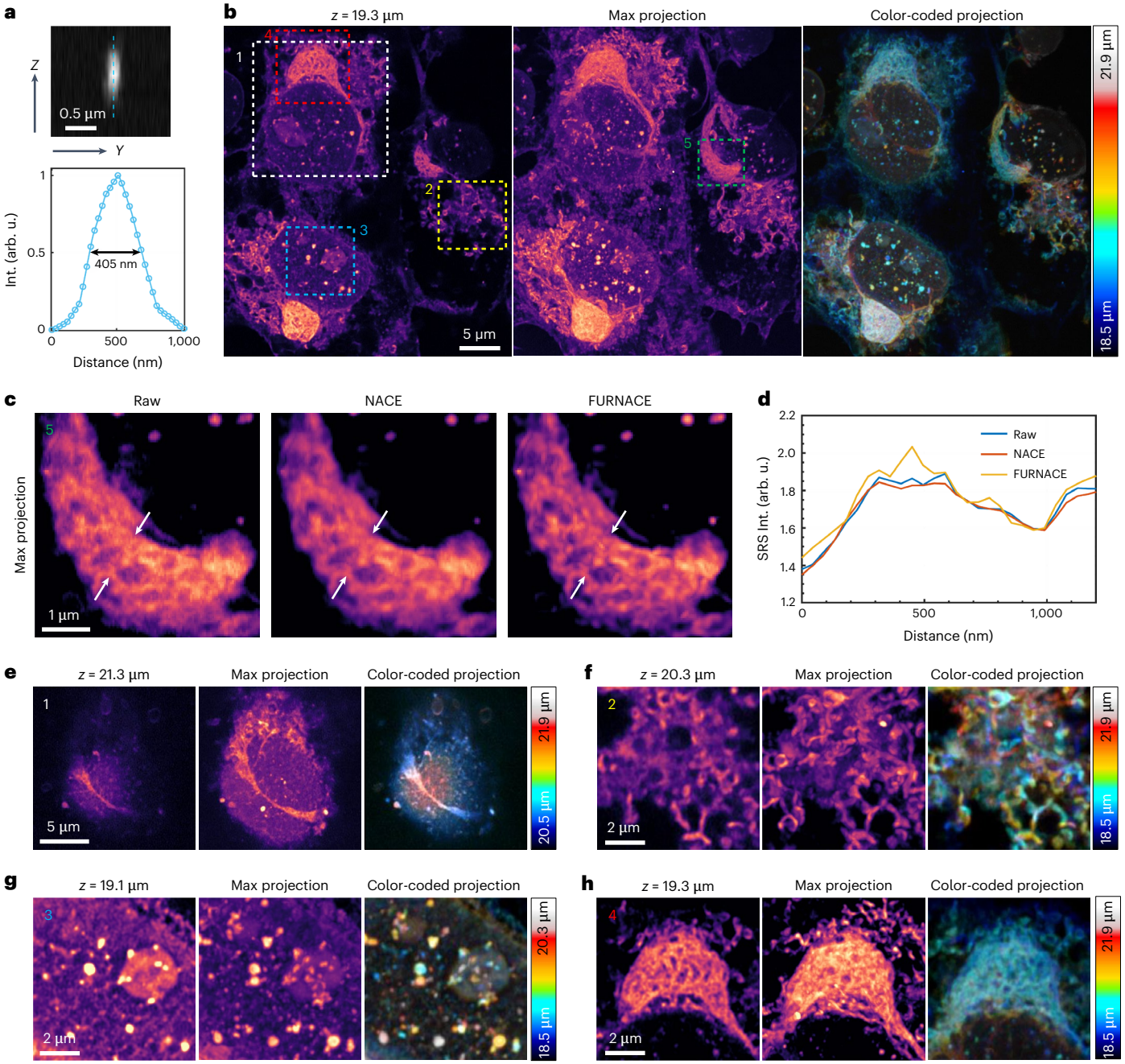

Fig. 4 | Three-dimensional URV-SRS imaging of ZIKV infected cells. a, 3D PSF (y–z cross section through the center) of visible SRS calibrated by a 30-nm gold nanoparticle. The axial line profile along the dashed line with full width at half maximum (FWHM) is shown. **b**, 3D imaging of ZIKV-infected cells, with a step size of 200 nm and a total range of 3.5 μm (z = 18.5–21.9 μm). A single slice at the center (z = 19.3 μm), axial maximum projection, and color-coded axial projection of all slices are shown. Three independent experiments were repeated with similar results. **c**, Zoom-in comparison between the Raw, NACE and FURNACE max projection images of the dashed box 5 in **b**. **d**, Line profiles between the two arrows in the Raw, NACE and FURNACE images. **e**, Zoom-in of the dashed box 1 in **c**, showing the top layers of a replication site wrapping the nucleus. **f**, Zoom-in of the dashed box 2 in **c**, showing the ER structure. **g**, Zoom-in of the dashed box 3 in **c**, showing the domain structures inside the nucleus. **h**, Zoom-in of the dashed box 4 in **c**, showing the virus-replication site. **e**–**h**, Each zoom-in panel contains a single-slice image, axial maximum projection and color-coded axial projection of the slices in the ranges shown in the look-up table on the right of each panel.

production heterogeneity stems from the variation of cell tolerance to fatty acid toxicity.

We further performed hyperspectral SRS on the same cells to provide high-content chemical information. Illustrated in Fig. 5d, we analyzed the raw hyperspectral data to produce maps highlighting the cell body, unsaturated fatty acids and saturated fatty acids, with their spectra displayed in Fig. 5e (Supplementary Fig. 12 and Supplementary Note 12). Maps of the same cells in Fig. 5b are shown in Fig. 5f. The cell body maps, mainly indicative of proteins and nucleic acids, showed a more uniform distribution throughout the cells. By contrast, unsaturated fatty acids were predominantly located along the cell membranes and at sites active in fatty acid expulsion. Saturated fatty acids had lower concentrations within the cells and mostly located at fatty acid extrusion sites. Increased membrane unsaturated fatty acid content has been reported as a stress response to internal free fatty acid production in *E. coli*, which may explain the substantially increased unsaturated

https://doi.org/10.1038/s41592-024-02575-1

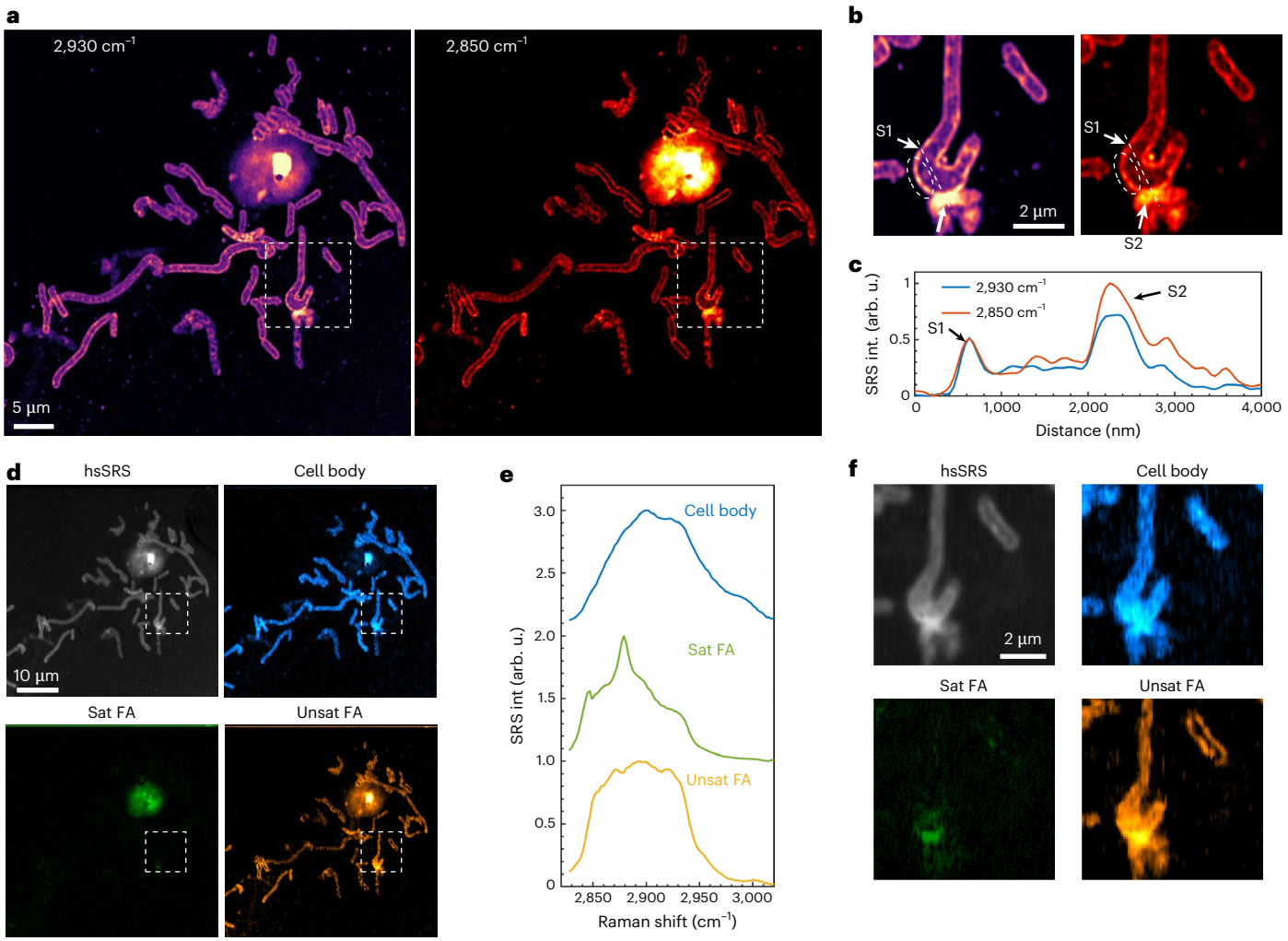

Fig. 5 | URV-SRS imaging fatty acid production inside single bacteria. a, Two-color URV-SRS imaging of engineered *E. coli* with fatty acid production. Three independent experiments were repeated with similar results. **b**, Zoom-in of the dashed box in **a**. **c**, Line profiles along the dashed line in **b**. **d**, Hyperspectral SRS (hsSRS, spectral sum shown) of the same FOV and spectral unmixing output maps, including cell body, saturated fatty acids (Sat FA) and unsaturated fatty acids (Unsat FA). **e**, Spectral references for the three-component unmixing, extracted directly from the raw hyperspectral image. **f**, Zoom-in of the same dashed region in the hyperspectral dataset, showing the raw hsSRS and chemical maps of cell body, sat FA and unsat FA.

membrane profile[50]. These spatial and spectral findings underscore the capability of URV-SRS to study the subcellular metabolic processes of bacteria at unprecedented resolution and specificity.

Broader applications of FURNACE

FURNACE is widely applicable to imaging modalities in which the system PSF is the product of multiple diffraction-limited PSFs, such as NIR SRS, multiphoton microscopy[51], image scanning microscopy[32] and super-resolution optical fluctuation imaging[33]. We compared FURNACE with existing computation-based resolution enhancement methods for these modalities, including Richardson–Lucy (R–L) deconvolution and A-Pod[25], as shown in Extended Data Fig. 9. Owing to the limited SNR of the raw image, R–L deconvolution introduced obvious artifacts by amplifying high spatial frequency noise and non-independent patterned noise. Meanwhile, because of the prior assumption of pointillism, A-Pod filtered out weak and continuous spatial features. In comparison, FURNACE suppresses noise before resolution enhancement and defines the spatial frequency cut-off, making it more robust against induced artifacts.

To demonstrate its broad applicability, we performed FURNACE resolution enhancement on NIR SRS imaging of SKOV3 cells at 2,930 cm^{-1}. Comparison between the raw (Extended Data Fig. 10a,b) and FURNACE output (Extended Data Fig. 10c,d) shows that FURNACE improved the resolution and unveiled structures inside both the cytoplasm (dashed box 1) and the nucleus (dashed box 2) that were obscured in the raw image. We note that the resolution enhancement is diffraction-limited and is bounded by the passband of the imaging system unless special sample conditions, such as sparse point sources, are incorporated. The FRC values showed consistent resolution across samples (Supplementary Fig. 13), reflecting the robustness of denoising and reweighting in the FURNACE algorithm.

Discussion

URV-SRS achieves high-content nanoscopic imaging of metabolites in natural cell environments. This achievement is based on the 50-fold increase in sensitivity, which enables the visualization of nanoscopic features that were previously obscured by noise. The resolution enhancement in URV-SRS is thus built on the increase of sensitivity, contrasting with most super-resolution vibrational imaging techniques that enhance resolution at the expense of sensitivity degradation. A comprehensive summary of different super-resolution coherent Raman imaging techniques is provided in Supplementary Table 1.

Our experimental investigations demonstrate that photodamage induced by femtosecond visible lasers can be mitigated through

extensive pulse chirping. By reducing peak power and increasing scanning speeds, we achieved biocompatible imaging at substantially higher power thresholds. Furthermore, chirping favors the detection of Raman signals over the broadband background owing to the matched narrow instantaneous excitation bandwidth in spectral focusing. Extending chirping to tens of picoseconds might provide additional SRS signal enhancements in the visible region by further increasing power limits and reducing non-Raman backgrounds, as demonstrated in a previous NIR SRS[52] study. It is noteworthy that, although the established power levels did not adversely affect cell morphology, they could impair cell functions, as supported by prior studies on longitudinal SRS imaging of bacterial colonies[48]. A more stringent condition, free of biological perturbations, could be established using fluorescent heat-shock stress reporters as indicators[53].

The NACE denoising algorithm, eliminating the need for explicit object or noise modeling, is particularly effective for removing local correlative noise in imaging modalities involving lock-in amplifiers. However, NACE suffers from computational speed drawbacks. Owing to the requirement of training multiple neural networks, the training speed is much slower than training a single network. During the prediction phase, the consensus equilibrium framework requires multiple iterations to converge, with each iteration involving predictions from all networks, resulting in further slowdowns. In our implementation, we incorporated 4 neural networks and used 10 iterations in the prediction phase, resulting in a total training time of ~12 h and a prediction time of ~10 seconds (using TensorFlow on an Nvidia RTX 4090 GPU). This is 4 times slower in training and 40 times slower in prediction than is a single neural network.

We highlight several limitations and possible future developments for URV-SRS. Owing to its short excitation wavelength and susceptibility to chromatic aberration, URV-SRS suffers from a limited sub-100-µm penetration depth, making it applicable only to 2D cell culture or thin tissue slices. Tissue clearance[54] and wavefront shaping[55] can be applied to address scattering and chromatic aberration to enable 3D imaging in thick tissue samples. The resolution of URV-SRS is diffraction-limited to ~80 nm. Expansion microscopy[56] could be explored to further enhance its resolution to the sub-20-nm level. The specificity of URV-SRS is limited to major metabolic species with high concentrations in the CH region. To enhance the specificity and sensitivity, pre-resonance Raman tag[57], which benefits from greater design flexibility in the visible window, can be introduced to image small molecules at ultrahigh sensitivity and specificity. URV-SRS can also be integrated with fluorescence nanoscopy to provide complementary nanoscopic imaging of fluorescently labeled proteins and non-fluorescent metabolic species, offering opportunities for nanoscopic multi-omics.

Online content

Any methods, additional references, Nature Portfolio reporting summaries, source data, extended data, supplementary information, acknowledgements, peer review information; details of author contributions and competing interests; and statements of data and code availability are available at https://doi.org/10.1038/s41592-024-02575-1.

References

1. Sahl, S. J., Hell, S. W. & Jakobs, S. Fluorescence nanoscopy in cell biology. *Nat. Rev. Mol. Cell Bio.* **18**, 685–701 (2017).
2. Betzig, E. et al. Imaging intracellular fluorescent proteins at nanometer resolution. *Science* **313**, 1642–1645 (2006).
3. Rust, M. J., Bates, M. & Zhuang, X. W. Sub-diffraction-limit imaging by stochastic optical reconstruction microscopy (STORM). *Nat. Methods* **3**, 793–795 (2006).
4. Hell, S. W. & Wichmann, J. Breaking the diffraction resolution limit by stimulated-emission — stimulated-emission-depletion fluorescence microscopy. *Opt. Lett.* **19**, 780–782 (1994).
5. Gustafsson, M. G. L. Surpassing the lateral resolution limit by a factor of two using structured illumination microscopy. *J. Microsc.* **198**, 82–87 (2000).
6. Giesen, C. et al. Highly multiplexed imaging of tumor tissues with subcellular resolution by mass cytometry. *Nat. Methods* **11**, 417–422 (2014).
7. Morato, N. M. & Cooks, R. G. Desorption electrospray ionization mass spectrometry: 20 years. *Acc. Chem. Res.* **56**, 2526–2536 (2023).
8. Ma, S. Y. et al. High spatial resolution mass spectrometry imaging for spatial metabolomics: advances, challenges, and future perspectives. *Trends Anal. Chem.* **159**, 116902 (2023).
9. Johnson, C. H., Ivanisevic, J. & Siuzdak, G. Metabolomics: beyond biomarkers and towards mechanisms. *Nat. Rev. Mol. Cell Bio.* **17**, 451–459 (2016).
10. Alexandrov, T. Spatial metabolomics: from a niche field towards a driver of innovation. *Nat. Metab.* **5**, 1443–1445 (2023).
11. Zumbusch, A., Holtom, G. R. & Xie, X. S. Three-dimensional vibrational imaging by coherent anti-Stokes Raman scattering. *Phys. Rev. Lett.* **82**, 4142–4145 (1999).
12. Freudiger, C. W. et al. Label-free biomedical imaging with high sensitivity by stimulated raman scattering microscopy. *Science* **322**, 1857–1861 (2008).
13. Zhang, D. L. et al. Depth-resolved mid-infrared photothermal imaging of living cells and organisms with submicrometer spatial resolution. *Sci. Adv.* **2**, e1600521 (2016).
14. Yonemaru, Y. et al. Super-spatial- and -spectral-resolution in vibrational imaging via saturated coherent anti-stokes raman scattering. *Phys. Rev. Appl.* **4**, 2676–2681 (2015).
15. Singh, A. K., Santra, K., Song, X. Y., Petrich, J. W. & Smith, E. A. Spectral narrowing accompanies enhanced spatial resolution in saturated coherent anti-Stokes Raman scattering (CARS): comparisons of experiment and theory. *J. Phys. Chem. A* **124**, 4305–4313 (2020).
16. Gong, L., Zheng, W., Ma, Y. & Huang, Z. W. Saturated stimulated-Raman-scattering microscopy for far-field superresolution vibrational imaging. *Phys. Rev. Appl.* **11**, 034041 (2019).
17. Würthwein, T., Irwin, N. & Fallnich, C. Saturated Raman scattering for sub-diffraction-limited imaging. *J. Chem. Phys.* **151**, 194201 (2019).
18. Gong, L., Zheng, W., Ma, Y. & Huang, Z. W. Higher-order coherent anti-Stokes Raman scattering microscopy realizes label-free super-resolution vibrational imaging. *Nat. Photonics* **14**, 115–122 (2020).
19. Fu, P. C. et al. Super-resolution imaging of non-fluorescent molecules by photothermal relaxation localization microscopy. *Nat. Photonics* **17**, 330–337 (2023).
20. Lv, X. B., Gong, L., Lin, S. L., Jin, P. & Huang, Z. W. Super-resolution stimulated Raman scattering microscopy with the phase-shifted spatial frequency modulation. *Opt. Lett.* **47**, 4552–4555 (2022).
21. Guilbert, J. et al. Label-free super-resolution chemical imaging of biomedical specimens. *Adv. Imaging* **1**, 011004 (2024).
22. Fantuzzi, E. M. et al. Wide-field coherent anti-Stokes Raman scattering microscopy using random illuminations. *Nat. Photonics* **17**, 1097–1104 (2023).
23. Qian, C. X. et al. Super-resolution label-free volumetric vibrational imaging. *Nat. Commun.* **12**, 3648 (2021).
24. Shi, L. X. et al. Super-Resolution vibrational imaging using expansion stimulated raman scattering microscopy. *Adv. Sci.* **9**, 2200315 (2022).
25. Jang, H. et al. Super-resolution SRS microscopy with A-PoD. *Nat. Methods* **20**, 448–458 (2023).
26. Bi, Y. L. et al. Near-resonance enhanced label-free stimulated Raman scattering microscopy with spatial resolution near 130 nm. *Light Sci. Appl.* **7**, 81 (2018).

27. Xiong, H. Q. et al. Stimulated Raman excited fluorescence spectroscopy and imaging. *Nat. Photonics* **13**, 412–417 (2019).
28. Xiong, H. Q. et al. Super-resolution vibrational microscopy by stimulated Raman excited fluorescence. *Light Sci. Appl.* **10**, 87 (2021).
29. Shou, J. W. et al. Super-resolution vibrational imaging based on photoswitchable Raman probe. *Sci. Adv.* **9**, eade9118 (2023).
30. Ao, J. et al. Photoswitchable vibrational nanoscopy with sub-100-nm optical resolution. *Adv Photonics* **5**, 066001 (2023).
31. Buzzard, G. T., Chan, S. H., Sreehari, S. & Bouman, C. A. Plug-and-play unplugged: optimization-free reconstruction using consensus equilibrium. *SIAM J. Imaging Sci.* **11**, 2001–2020 (2018).
32. Müller, C. B. & Enderlein, J. Image scanning microscopy. *Phys. Rev. Lett.* **104**, 198101 (2010).
33. Dertinger, T., Colyer, R., Vogel, R., Enderlein, J. & Weiss, S. Achieving increased resolution and more pixels with superresolution optical fluctuation imaging (SOFI). *Opt. Express* **18**, 18875–18885 (2010).
34. Koho, S. et al. Fourier ring correlation simplifies image restoration in fluorescence microscopy. *Nat. Commun.* **10**, 3103 (2019).
35. Dabov, K., Foi, A., Katkovnik, V. & Egiazarian, K. Image denoising with block-matching and 3D filtering. In *Proc. SPIE 6064, Image Processing: Algorithms and Systems, Neural Networks, and Machine Learning* **6064**, 606414 (SPIE, 2006).
36. Krull, A., Buchholz, T. O. & Jug, F. Noise2Void-learning denoising from single noisy images. In *Proc. IEEE IEEE/CVF Conference on Computer Vision and Pattern Recognition* 2124–2132 (CVF, 2019).
37. Xu, J. et al. Noisy-as-Clean: learning self-supervised denoising from corrupted image. *IEEE Trans. Image Process.* **29**, 9316–9329 (2020).
38. Weigert, M. et al. Content-aware image restoration: pushing the limits of fluorescence microscopy. *Nat. Methods* **15**, 1090–1097 (2018).
39. Wang, Z., Bovik, A. C., Sheikh, H. R. & Simoncelli, E. P. Image quality assessment: From error visibility to structural similarity. *IEEE Trans. Image Process.* **13**, 600–612 (2004).
40. Boyd, R. W. *Nonlinear Optics* 4th edn (Academic Press, 2020).
41. Rossignol, E. D., Peters, K. N., Connor, J. H. & Bullitt, E. Zika virus induced cellular remodelling. *Cell Microbiol.* **19**, e12740 (2017).
42. Miron, E. et al. Chromatin arranges in chains of mesoscale domains with nanoscale functional topography independent of cohesin. *Sci. Adv.* **6**, eaba8811 (2020).
43. Li, P. et al. The RNA polymerase of cytoplasmically replicating Zika virus binds with chromatin DNA in nuclei and regulates host gene transcription. *Proc. Natl Acad. Sci. USA* **119**, e2205013119 (2022).
44. Tan, Y., Lin, H. & Cheng, J.-X. Profiling single cancer cell metabolism via high-content SRS imaging with chemical sparsity. *Sci. Adv.* **9**, eadg6061 (2023).
45. Saxena, N. & Chandra, N. C. Cholesterol: a prelate in cell nucleus and its serendipity. *Curr. Mol. Med.* **20**, 692–707 (2020).
46. Lee, S. Y. et al. A comprehensive metabolic map for production of bio-based chemicals. *Nat. Catal.* **2**, 18–33 (2019).
47. Xiao, Y., Bowen, C. H., Liu, D. & Zhang, F. Z. Exploiting nongenetic cell-to-cell variation for enhanced biosynthesis. *Nat. Chem. Biol.* **12**, 339–344 (2016).
48. Tague, N. et al. Longitudinal single-cell imaging of engineered strains with stimulated raman scattering to characterize heterogeneity in fatty acid production. *Adv. Sci.* **10**, 2206519 (2023).
49. Willdigg, J. R. & Helmann, J. D. Mini review: bacterial membrane composition and its modulation in response to stress. *Front. Mol. Biosci.* **8**, 634438 (2021).
50. Lennen, R. M. et al. Membrane stresses induced by overproduction of free fatty acids in *Escherichia coli*. *Appl. Environ. Microb.* **77**, 8114–8128 (2011).
51. Helmchen, F. & Denk, W. Deep tissue two-photon microscopy. *Nat. Methods* **2**, 932–940 (2005).
52. Koike, K., Smith, N. I. & Fujita, K. Spectral focusing in picosecond pulsed stimulated Raman scattering microscopy. *Biomed. Opt. Express* **13**, 995–1004 (2022).
53. Ceroni, F. et al. Burden-driven feedback control of gene expression. *Nat. Methods* **15**, 387–393 (2018).
54. Wei, M. et al. Volumetric chemical imaging by clearing-enhanced stimulated Raman scattering microscopy. *Proc. Natl Acad. Sci. USA* **116**, 6608–6617 (2019).
55. Lin, P. et al. Volumetric chemical imaging in vivo by a remote-focusing stimulated Raman scattering microscope. *Opt. Express* **28**, 30210–30221 (2020).
56. Wassie, A. T., Zhao, Y. X. & Boyden, E. S. Expansion microscopy: principles and uses in biological research. *Nat. Methods* **16**, 33–41 (2019).
57. Wei, L. et al. Super-multiplex vibrational imaging. *Nature* **544**, 465–470 (2017).

Methods

Visible SRS microscope with extensive pulse chirping

The setup, as depicted in Fig. 1a, employs a dual output synchronized tunable femtosecond laser system (Insight X3, Spectra Physics) for its operation. The outputs of the laser were tuned to wavelengths of 906 nm and 1,045 nm, respectively, and each was frequency-doubled to 453 nm and 523 nm through second harmonic generation, achieving approximately 10% conversion efficiency. The intensity of the Stokes beam was modulated at 2.4 MHz using an acousto-optic modulator (AOM, M1205-P80L-0.5, Isomet) for the detection of the pump-probe signal. The two beams were combined using a dichroic mirror (DI03-R488/561-t1-25×36, Semrock) and were propagated simultaneously to the microscope. To linearly chirp the femtosecond pulses, three 15-cm high-dispersion glass rods (SF57, Schott) were placed in the common path. Additionally, one 15-cm glass rod was positioned in the Stokes path to ensure parallel chirping between the two beams, which is essential for achieving high spectral resolution through spectral focusing. The merged beams were then directed to a custom-built laser-scanning microscope, equipped with galvo scanners (GVS001, Thorlabs). A pair of 1.49-NA oil-immersion ×100 objectives (UAPON 100XOTIRF, Olympus) was utilized for tightly focused laser scanning and forward light collection. The pump beam, carrying the stimulated Raman loss signal after interacting with the sample, was isolated by a bandpass filter (ET450/50m, Chroma) and detected by a custom-built tuned amplifier photodiode (S3994-01, Hamamatsu) operating at 2.4 MHz. This filtered signal was then fed to a lock-in amplifier (UHFLI, Zurich Instruments) to extract the SRS signal. The output signal was collected by a data acquisition card (PCIE-6363, National Instruments). To obtain hyperspectral imaging, a motorized linear stage was installed in the Stokes optical path to scan the temporal delays for spectral focusing. A piezo nano-positioner (Nano-LP200, Mad City Labs) was used for 3D imaging, which accurately adjusted the axial position of the sample after each 2D scan to construct the volume in a layer-by-layer manner. All the programs for hardware control and data acquisition were custom-written in LabView (National Instruments).

Simultaneous SRS and confocal fluorescence acquisition

We installed a quarter wave plate and a polarizing beam splitter in front of the galvo mirrors to collect the de-scanned epi signals. A confocal pinhole with the size of ~1.2 Airy Unit was placed on the sample conjugate plane to reject the out-of-focus fluorescence. A photomultiplier tube (PMT, H16722-40, Hamamatsu) was used to collect the fluorescence signal. Confocal fluorescence and SRS imaging of the same FOV were acquired in a sequential manner. We first blocked the pump and set the 523 nm Stokes laser to 50 µW for excitation and collected the confocal fluorescence emission signals. Subsequently, the pump and Stokes powers were both increased to 10 mW to obtain SRS images. This sequential protocol avoids the photobleaching of the fluorophores by the SRS lasers.

Data acquisition and pre-processing

For all experiments, we determined the laser power on the sample by measuring the power before the objective and multiplying it by the pre-calibrated objective transmission. For imaging using 30-nm gold nanoparticles, the pump and Stokes were both set to 50 µW with a pixel dwell time of 10 µs and pixel size of 30 nm. For single-color visible SRS imaging, all the measurements were acquired with 2 µs pixel dwell time and 45 nm pixel size. The laser powers and the number of continuous repeated measurements were 10 mW for both beams and 10 frames for SKOV3 and VERO mammalian cells (both mock and ZIKV-infected), and 8 mW for both beams and 10 frames for bacterial cells NT71. Drift correction with Fast4DReg[58] was applied to all the raw image sequence before frame averaging. To generate noisier–noisy images for FURNACE processing, the total frame number was reduced to five by averaging two adjacent frames. For hyperspectral SRS imaging, the acquisition conditions were changed to a 3-µs pixel dwell time and 90-nm pixel size. A total of 100 hyperspectral frames were taken in each hyperspectral stack to cover the entire CH region.

NACE denoising

We describe the raw image sequence, containing N repeated high-speed measurements of the same FOV, as $[\mathbf{t_1}, \mathbf{t_2}, \ldots, \mathbf{t_N}]$. The raw SRS output image ($\mathbf{y} \in \mathbb{R}^n$) is acquired by averaging all the frames, and is connected to the clean object $\mathbf{x} \in \mathbb{R}^n$ through a linear relationship:

$$\mathbf{y} = \frac{\sum_{i=1}^{N} \mathbf{t_i}}{N} = \mathbf{x} + \mathbf{n_o},$$

where $\mathbf{n_o}$ is observed noise with unknown statistical distribution. The goal of the NACE algorithm is to find the best estimate ($\hat{\mathbf{x}}$) using a single time sequence ($[\mathbf{t_1}, \mathbf{t_2}, \ldots, \mathbf{t_N}]$) without having access to ground truth with SNR higher than that of $\mathbf{y}$. The algorithm consists of three steps, including (1) generating noisier–noisy training data; (2) using various noisier–noisy image pairs to train NAC denoisers at different SNR levels; and (3) ensemble prediction through consensus equilibrium for SNR-matched noisy image denoising.

First, we produce experimental noisier images $\mathbf{z_k}$ from the raw image sequence $[\mathbf{t_1}, \mathbf{t_2}, \ldots, \mathbf{t_N}]$ as:

$$\mathbf{z_k} = \frac{\sum_{i=1}^{k} \mathbf{t_i}}{k} = \mathbf{y} + \mathbf{n_{ak}},$$

where $k = 1, \ldots, N-1$ represents the number of averaged frames. By reducing the number of frames from N to k, $\mathbf{y}$ received additional noise ($\mathbf{n_{ak}}$) sharing the same behaviors as $\mathrm{n_o}$. A series of noisier images with different added noise levels ($\sigma_{\mathrm{n_{ak}}}$) are generated by changing k. Although not having a single case with perfectly matched added noise levels (that is, $\sigma_{\mathrm{n_{ak}}} = \sigma_{\mathrm{n_o}}$), this strategy produced noisier images with $\sigma_{\mathrm{n_{ak}}}$ both higher and lower than $\sigma_{\mathrm{n_o}}$.

In the second step, we use pairs of $\mathbf{y} - \mathbf{z_k}$ to perform supervised training of deep neural networks, which learns the image priors shared across $\mathbf{x}$, $\mathbf{y}$ and $\mathbf{z_k}$, and non-independent noise behaviors of $\mathbf{n_{sk}}$, shared with $\mathbf{n_o}$. The network structure of each NAC is based on residual versions of the U-Net[38] in 2D. In brief, the network is a three-layer encoder–decoder architecture. Each encoding layer contains a 1×1 convolution layer, six 5×5 convolution layers, and a max-pooling layer, while each decoding layer contains an upsampling, six convolution layers and a concatenation layer. Upon unsampling, the data are connected to the input to perform residual learning. The network was implemented in Tensorflow and trained on a single graphics card (RTX 4090, Nvidia). For each demonstration, we measured approximately six different FOVs and performed data augmentation (rotate and flip) to increase the training data size. We randomly generated 1,000 patches of noisier–noisy image pairs for training, with each path having a size of 128×128 pixels. The training time for each NAC denoiser was around 3 h. Using multiple pairs of $\mathbf{y}-\mathbf{z_k}$ at different added noise levels, we trained a series of individual NACs despite mismatched SNRs.

Finally, we leverage the CE[31] framework that combines multiple SNR-mismatched NAC denoisers in a federated manner to achieve SNR-matched denoising. We treat the inverse problem of denoising as:

$$\hat{\mathbf{x}} = \underset{\mathbf{x} \in \mathbb{R}^n}{\arg\min} \frac{1}{2\sigma_{\mathrm{n_o}}^2} \|\mathbf{y} - \mathbf{x}\|^2 + \sum_{i=1}^{K} \mathrm{h_i}(\mathbf{x}),$$

where $\mathrm{h_i}(\mathbf{x})$ represents a regularization function (that is prior model) and K is the total number of the functions. Here, each regularization function is an individually trained NAC neural network, whose proximal map can be expressed in the CE framework as the operator:

$$F_i(\mathbf{v}_i) = \mathrm{NAC}(\mathbf{v}_i \text{ with } \sigma_{n_{ak}}).$$

Combining with the proximal map of the data fidelity term:

$$F_{K+1}(\mathbf{v}_{K+1}) = \arg\min_{\mathbf{x}\in\mathbb{R}^n} \frac{1}{2\sigma_{n_o}^2}\|\mathbf{y}-\mathbf{x}\|^2 + \frac{1}{2\sigma_{n_o}^2}\|\mathbf{v}_{K+1}-\mathbf{x}\|^2,$$

we can write the compact form of CE as the combination of an operator module:

$$F(w) = \begin{bmatrix} F_1(w_1) \\ \vdots \\ F_{K+1}(w_{K+1}) \end{bmatrix} \text{where } w = \begin{bmatrix} w_1 \\ \vdots \\ w_{K+1} \end{bmatrix},$$

and an averaging module:

$$G_\mu(w) = \begin{bmatrix} \bar{w} \\ \vdots \\ \bar{w} \end{bmatrix} \text{where} \bar{w} = \sum_{i=1}^{K+1} \mu_i w_i,$$

where $\mu_i = \frac{p_i}{\sum_{i=1}^{K+1} p_i}$ is the weight of each agent, $p_{k+1} = \sum_{i=1}^{K} p_i$, and $p_i = \exp\left(-\frac{(\sigma_{n_{ak}}-\sigma_{n_0})^2}{2\sigma_{n_0}^2}\right)$

The solution is found iteratively when F(w) = G(w). Pseudo code for solving the CE problem is provided in Supplemental Note 7.

Fourier reweighting

The system PSF of SRS is the multiplication of two co-localized, tightly focused Gaussian PSFs ($PSF_{SRS} = PSF_p \times PSF_S$) that can be approximated as a quadratic Gaussian function. Consequently, it shows a rapid attenuation of higher spatial frequencies within the support of the passband. The ratio between the FWHM and the cut-off frequency is thus less than that of a conventional Gaussian PSF. Because the resolvability of two adjacent features is determined by the full frequency support, it is reasonable to reshape the OTF profile and amplify the contributions from high spatial frequencies to fully leverage the attainable spatial resolution. We implement spatial frequency amplification in the Fourier domain by multiplying the Fourier image with the following function:

$$W(\boldsymbol{\kappa}) = \frac{OTF_P(n\boldsymbol{\kappa})}{OTF_{SRS}(\boldsymbol{\kappa}) + \varepsilon}, \boldsymbol{\kappa} < \Delta_P + \Delta_S,$$

where $n = \frac{\Delta_P + \Delta_S}{\Delta_P}$, $\varepsilon \ll 1$ is an adjustable constant to avoid amplifying high-frequency noise, and OTF_P, OTF_{SRS} are experimentally calibrated by measuring the PSFs of the pump and SRS. For detecting weak objects, ε can be toned up to avoid the object being overwhelmed by ringing artifacts at the expense of sacrificing effective resolution.

Spatial resolution benchmarking through Fourier ring correlation

We use one-image FRC to benchmark the spatial resolution by accounting for both the PSF and SNR of the image[34]. It splits an image into sub-image pairs by subsampling, calculates the normalized cross-correlation between the Fourier image pairs at different spatial frequencies, and finds the cut-off spatial frequency as the cross correlation reduces to 1/7. Because the sub-images measure the same FOV with independent added noise, levels of the cross correlation are linked to the spatial frequencies of the whole image and SNR.

Spectral unmixing through pixel-wise LASSO

The raw hyperspectral SRS are 3D data stacks with a high-dimensional SRS spectrum at each spatial pixel. To extract concentration maps of metabolites from the hyperspectral image, we use pixel-wise LASSO for spectral unmixing. First, we measure SRS spectra of standard samples of BSA, triglyceride, cholesterol, glucose and RNA to represent the target metabolites of proteins, lipids, cholesterol, carbohydrates and nucleic acids, respectively. To overcome spectral cross-talks between chemical species with overlapped Raman peaks, we add an L1-norm sparsity regularization to the concentration vector at each pixel. This 'chemical sparsity' prior assumes that each pixel is dominated by only a few pure components under high-resolution imaging of a heterogeneous cell environment. Details of the algorithm implementation and validation are included in a previous work[44].

Sample preparation

Gold nanoparticles for PSF measurement. We prepared gold nanoparticles using an established citrate reduction method[59], leading to particle diameters of around 30 nm. The diameters were well below the diffraction limit of the visible SRS system, such that the PSF could be directly measured without the need for deconvolution. We spin-coated 10 µl of nanoparticle colloidal suspension onto a coverslip to form sparse single particles. The particles were then immersed in oil to ensure refractive index matching and sandwiched by another coverslip for the PSF measurement.

SKOV3 cancer cells. SKOV3 (catalog no. HTB-77) cells were purchased from the American Type Culture Collection. The cells were cultured in high-glucose DMEM supplemented with 10% FBS and penicillin–streptomycin. The cells were maintained in a humidified incubator with a 5% CO_2 supply at 37 °C. Cells were directly grown on 22×22 No. 1 coverslips. Before the experiment, cells were fixed by formalin and sandwiched by another coverslip, enabling the use of oil-immersion objectives for high-resolution SRS imaging.

SJSA-1 bone cancer cells with fluorescence staining. SJSA-1 cells (CRL-2098) were purchased from American Type Culture Collection. The cells were cultured in a glass-bottom dish with RMPI 1640 (Thermo Fisher Scientific) with 10% FBS and penicillin–streptomycin. The cells were incubated with 50 µM NBD-label phosphatase activity reporter (NBD-Phos-CN(S)) for 1 h for fluorescence imaging. Before the imaging experiment, cells were fixed by formalin, and 1.2NA water immersion objectives were used to directly image cells in the culture dish.

Vero E6 cells with Zika virus infection. Vero E6 cells (CRL-1586 from American Type Culture Collection) were maintained in Minimum Essential Media (MEM, Gibco) with 10% FBS (Sigma). The Zika virus ZIKV PRVABC59 (2015 Puerto Rico strain, GenBank KZ087101.2) was obtained from Biodefense and Emerging Infections Research Resources Repository (BEI Resources). Cells were infected with the Zika virus at a multiplicity of infection (MOI) of 5 for 1 h. Cells were then washed 3 times to remove remaining extracellular viruses and were fed with fresh MEM. Cells in the control group were mock-infected. After 48 h, all cells were fixed 3 times by 2.5% glutaraldehyde, 1.25% foscarnet, 0.03% picric acid in 100 mM sodium cacodylate for 1 h, 1% OsO_4, 1.5% $KFeCN_6$ for 30 min and 1% uranyl acetate for 30 min, respectively. Cells were grown on No. 1 coverslips and were sandwiched by another coverslip for SRS imaging.

Chemical synthesis for antiviral compounds. CMLD013694, CMLD013695 and CMLD013697 were synthesized as described in Supplementary Note 11 and were submitted to the BU-CMD compound collection (https://www.bu.edu/cmd/).

Fatty acid production E. coli strains. The *E. coli* strains (AbTE*-FV50) were derived from Tague et al.[48]. For SRS imaging of fatty acid production from single bacteria, precultures were grown overnight in Luria Bertani (LB) medium with antibiotics for plasmid maintenance, as described in Tague et al.[48]. The cultures were grown in 3 ml M9 medium

(M9 salts, 2 mM $MgSO_4$ and 100 µl $CaCl_2$) and 2% glucose at 37 °C with 200 r.p.m. shaking. Then, 500 µM of IPTG was added to induce thioesterase expression until the culture reached an optical density at 600 nm of 0.6. The cultures were further grown at the same incubation conditions for 24 h. To perform the SRS experiment, samples were placed on 3% agarose pads containing M9 medium and sandwiched between No. 1 coverslips to immobilize the cells.

Reporting summary

Further information on research design is available in the Nature Portfolio Reporting Summary linked to this article.

Data availability

Example datasets for FURNACE and spectral unmixing are available at the Cheng Lab GitHub page (https://github.com/buchenglab). Larger raw datasets are available on figshare[60].

Code availability

All relevant code, including NACE denoising, Fourier reweighting and spectral unmixing, can be accessed at the Cheng Lab GitHub page (https://github.com/buchenglab).

References

58. Pylvänäinen, J. W. et al. Fast4DReg-fast registration of 4D microscopy datasets. *J. Cell Sci.* **136**, jcs260728 (2023).
59. Kimling, J. et al. Turkevich method for gold nanoparticle synthesis revisited. *J. Phys. Chem. B* **110**, 15700–15707 (2006).
60. Lin, H. Raw data for URV-SRS. *figshare* https://doi.org/10.6084/m9.figshare.26970583 (2024).

Acknowledgements

We thank C. A. Bouman for the discussion on the NACE denoising algorithm, N. Tague for the discussion on the bacterial fatty acid production results and L. Brown at BU-CMD for the help with antiviral compound curation. This work was supported by the Office of Science (BER) at the U.S. Department of Energy (DE-SC0019387 to M.J.D. and J.-X.C.), NIH R35 GM136223, R01 EB032391, R01 EB035429, R01 AI141439, R01 CA224275 to J.-X.C., R35 GM 118173 to J.A.P., Jr., and in part by grant number 2023-321163 from the Chan Zuckerberg Initiative DAF, an advised fund of Silicon Valley Community Foundation.

Author contributions

H.L. and J.-X.C. conceived the project. H.L. and L.W. constructed the extensively chirped visible SRS system. H.L. developed and implemented the FURNACE algorithm. Y.T. prepared SKOV3 cells and performed NIR SRS experiments for ZIKV-infected VERO cells. S.S. and J.C. provided ZIKV-infected, mock and drug-treated VERO cells. G.D. performed noise correlation analysis. J.-B.L. and M.J.D. provided fatty acid-producing *E. coli* strains. H.H. provided the SJSA-1 cells with fluorescence staining. J.A.P., Jr. and T.J.R. synthesized and provided antiviral compounds. H.L. and J.-X.C. wrote the manuscript with inputs and approval from all authors. J.-X.C. and L.T. supervised the project.

Competing interests

The authors declare no competing interests.

Additional information

Extended data is available for this paper at https://doi.org/10.1038/s41592-024-02575-1.

Supplementary information The online version contains supplementary material available at https://doi.org/10.1038/s41592-024-02575-1.

Correspondence and requests for materials should be addressed to Ji-Xin Cheng.

Peer review information *Nature Methods* thanks Natalie Belsey, Minbiao Ji, Dimitrios Tsikritsis and the other, anonymous, reviewer(s) for their contribution to the peer review of this work. Primary Handling Editor: Rita Strack, in collaboration with the *Nature Methods* team. Peer reviewer reports are available.

https://doi.org/10.1038/s41592-024-02575-1

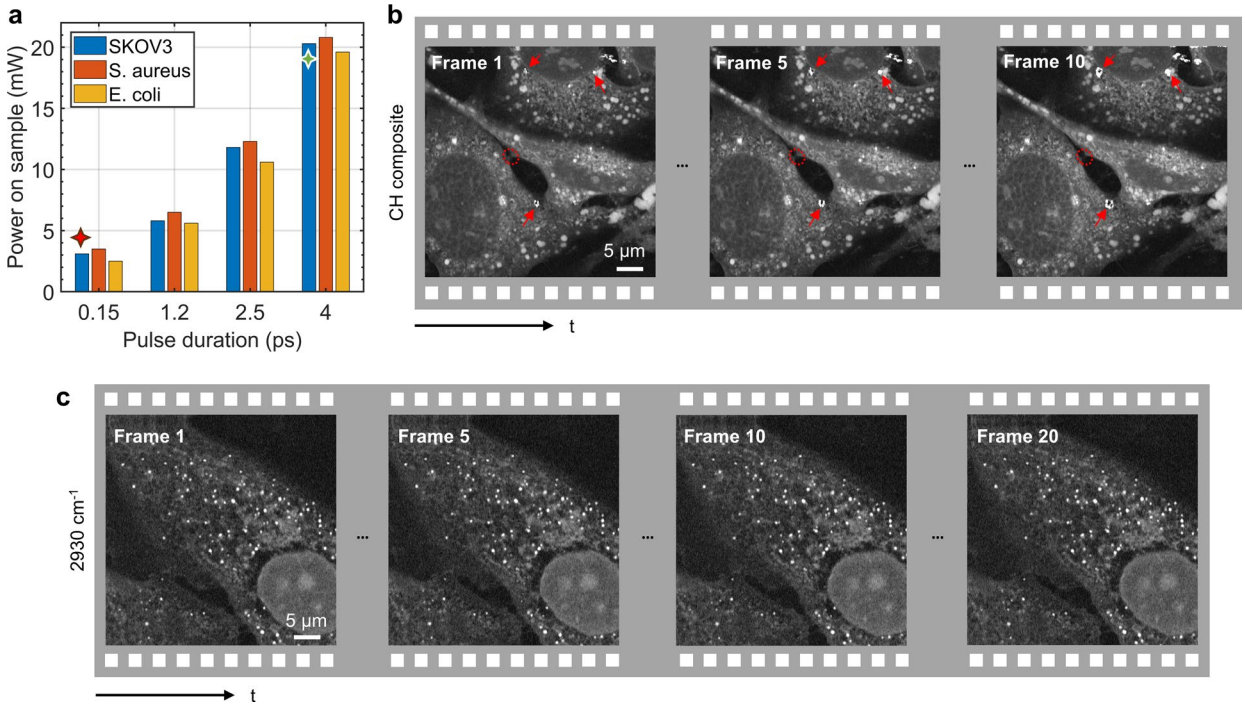

Extended Data Fig. 1 | Phototoxicity of visible SRS on biological samples under different pulse durations. (**a**) Damage threshold for three different cells under 4 different pulse chirping (duration) conditions. (**b**) SRS imaging (CH composite) of SKOV3 ovarian cancer cell with 0.15 ps laser at the power condition marked as the red asterisk in (a). Frames 1, 5 and 10 from 10 consecutive acquisitions are shown. Arrows show ionization photodamage and the circle indicate cell shrinkage induced by photodamage. 3 independent experiments were repeated with similar results.

https://doi.org/10.1038/s41592-024-02575-1

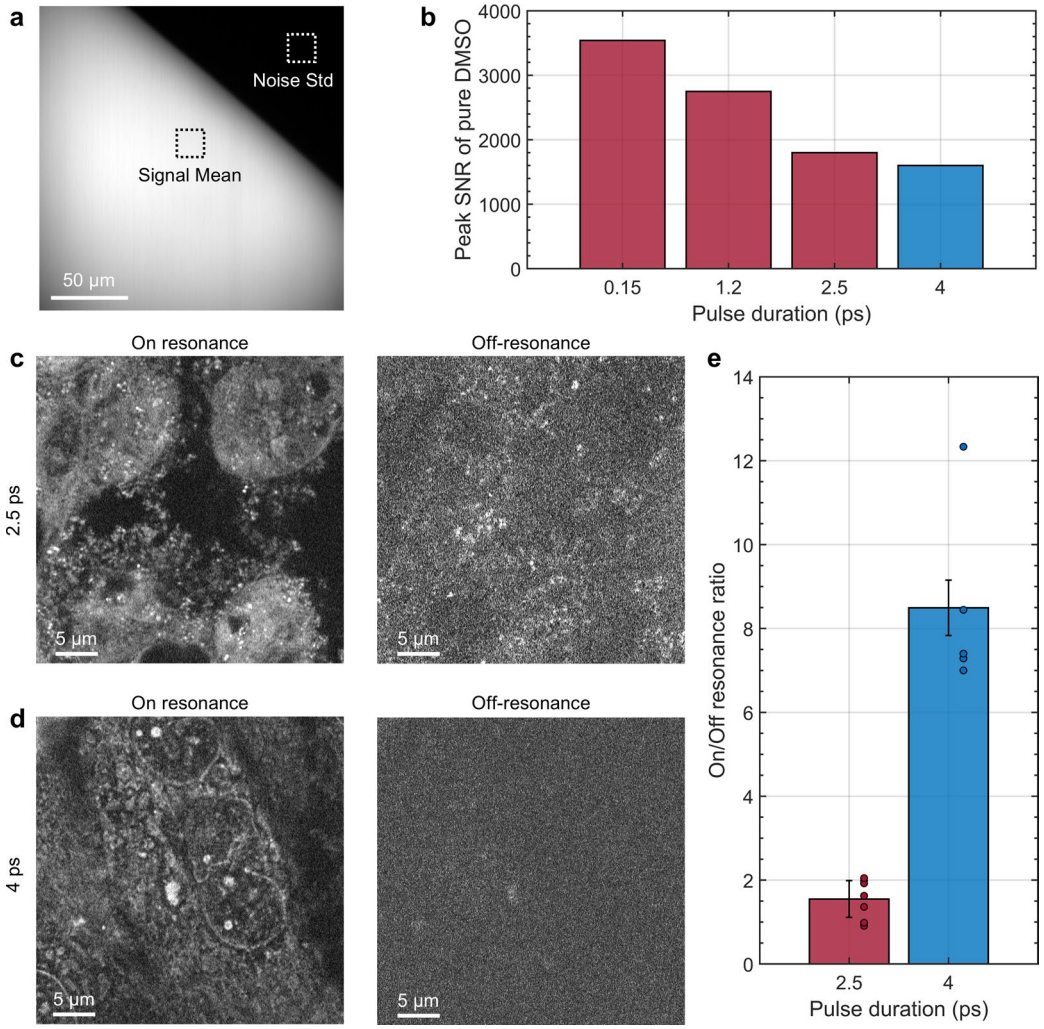

Extended Data Fig. 2 | Change of SRS signal intensity and off- resonance background under different pulse durations. (**a**) Visible SRS imaging of pure DMSO for SRS peak signal-to- noise ratio (SNR) measurement. Peak signal is the mean pixel values in the foreground dashed box, while the noise is quantified as the standard deviation in the background dashed box (n = 400 pixels for both boxes). (**b**) PSNR under different pulse durations. Average on-sample powers were fixed to 10 mW for pump and 10 mW for Stokes. (**c, d**) Visible SRS imaging of SJSA-1 bone cancer cells at Raman on resonance (2930 cm^{-1}) and off-resonance (2800 cm^{-1}) under 2.5 ps and 4 ps chirping conditions. (**e**) Ratio between Raman on and off resonance signals in cells. Datapoints represent average values from individual cells. n = 7 for 2.5 ps condition and 5 for 4 ps condition.

https://doi.org/10.1038/s41592-024-02575-1

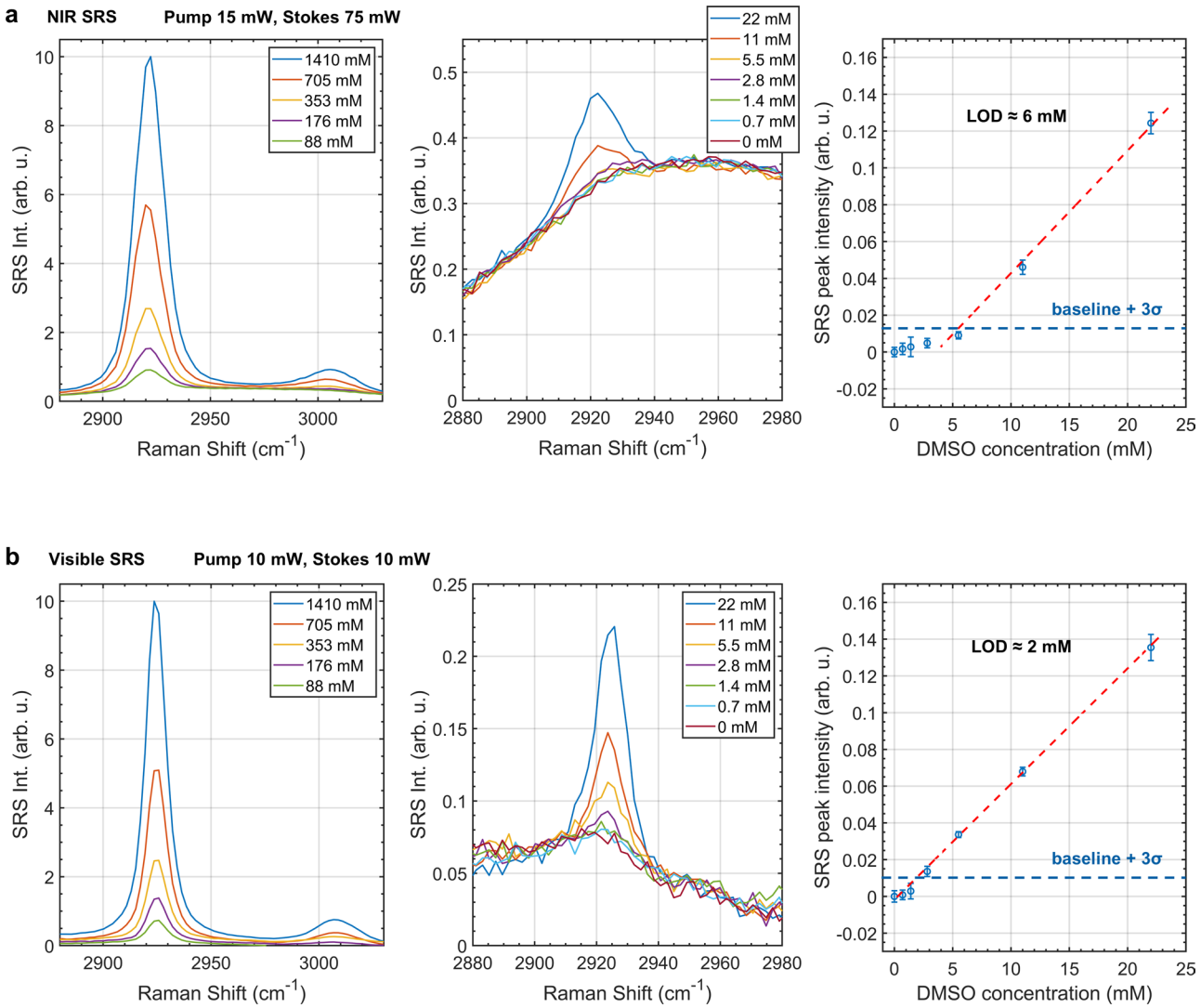

Extended Data Fig. 3 | Limit of detection (LOD) for NIR SRS and visible SRS under the biocompatible power limits. (**a**) NIR SRS spectra of DMSO serial dilution in water. Peak intensities versus DMSO concentrations were plotted and linearly fitted along the sloped dotted line. LOD was calculated as the linear fitting concentration at baseline intensity + 3σ (horizontal dotted line value), where baseline intensities were the mean values at zero concentrations and σ were the noise levels measured as the standard deviation in a background area (n = 400 pixels). (**b**) Visible SRS measurements of the same samples, together with the linearity curve to benchmark the LOD. Values of the LOD are shown in corresponding linear fitting plots.

https://doi.org/10.1038/s41592-024-02575-1

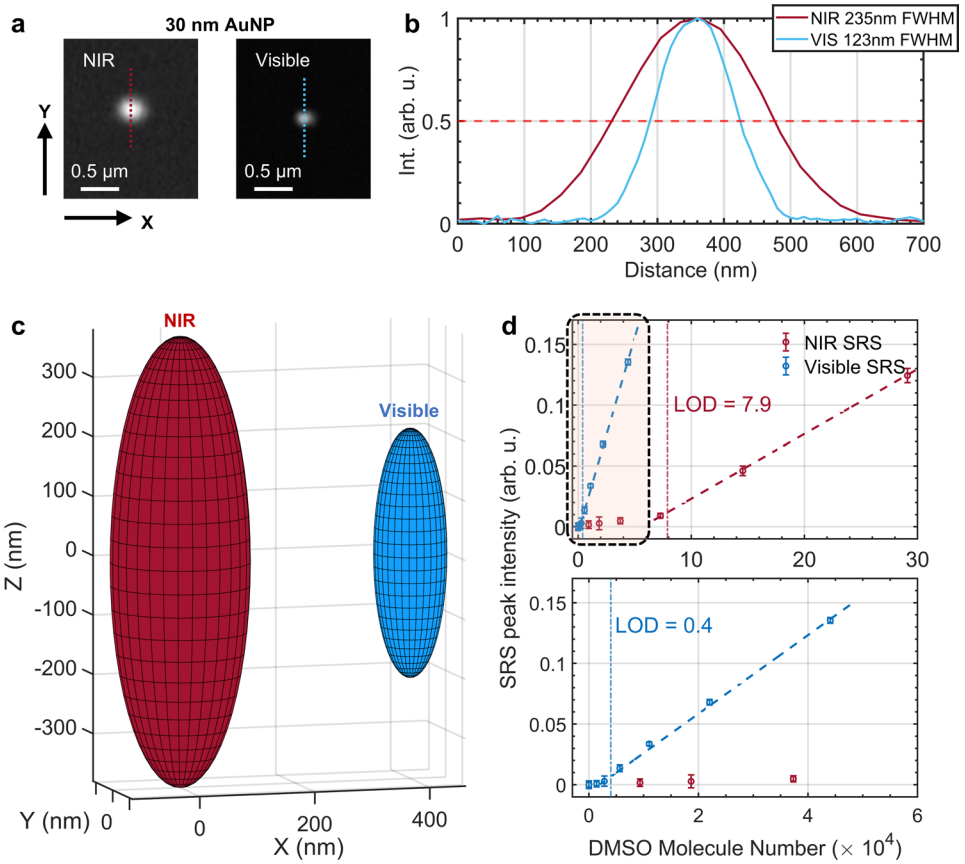

Extended Data Fig. 4 | Calculation of excitation volume for visible and NIR SRS. (**a**) Pump-probe signal of 30 nm AuNP using NIR and visible SRS. (**b**) Line profiles along the dotted lines in (a) with FWHM measurement. (**c**) Three-dimensional representation of the SRS PSF as a surface plot corresponding to the half of its maximum value. (**d**) DMSO detection limit for visible SRS and NIR SRS in terms of absolute number of molecules. Zoom-in of the shaded region on the top panel is shown on the bottom panel.

https://doi.org/10.1038/s41592-024-02575-1

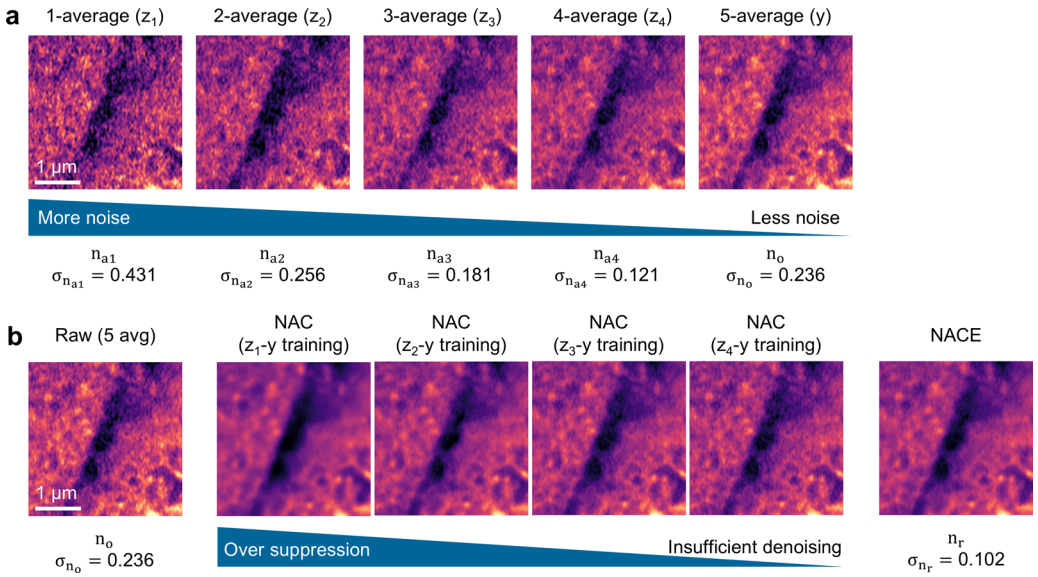

Extended Data Fig. 5 | Example of NACE data generation and denoising performance. (**a**) Examples of noisier images (z_1, …, z_4) and the noisy raw image (y) by changing the number of averaged frames. (**b**) Denoising of the raw image (y) using individual NACs and NACE. n_a, added noise; n_o, observed noise; n_r, residual noise.

https://doi.org/10.1038/s41592-024-02575-1

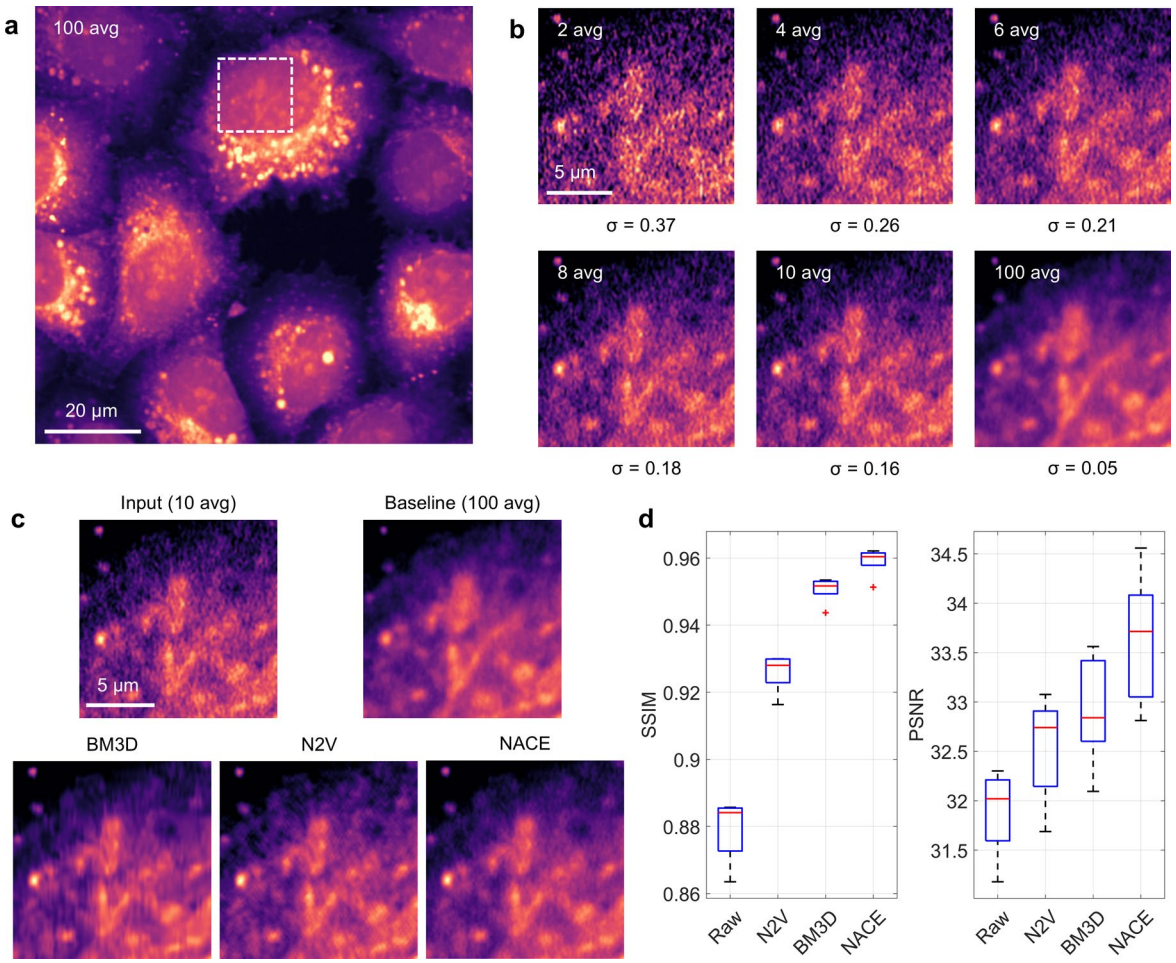

Extended Data Fig. 6 | Validating the performance of NACE denoising using datasets with high-SNR baseline. (**a**) Average of a 100-frame time sequence used as the ground truth. (**b**) Zoom-in of the dashed box in (a) with different number of averages, including 2, 4, 6, 8, 10 and 100. Measured noise levels are shown under each image. (**c**) Denoising of 10-average raw image using unsupervised/self- supervised denoiser (NACE, BM3D, N2V). (**d**) Quantification of denoising performance. Box plots (n = 5) show the structural similarity index (SSIM) and peak signal to noise ratio (PSNR) (the higher is better) between the raw, denoising outputs and the ground truth. The boxes indicate interquartile range (IQR), the red lines show medians, the black lines represent whiskers which extend to 1.5 times of the IQR, and the red data points are the outliers exceeding the whiskers. 3 independent experiments were repeated with similar results.

https://doi.org/10.1038/s41592-024-02575-1

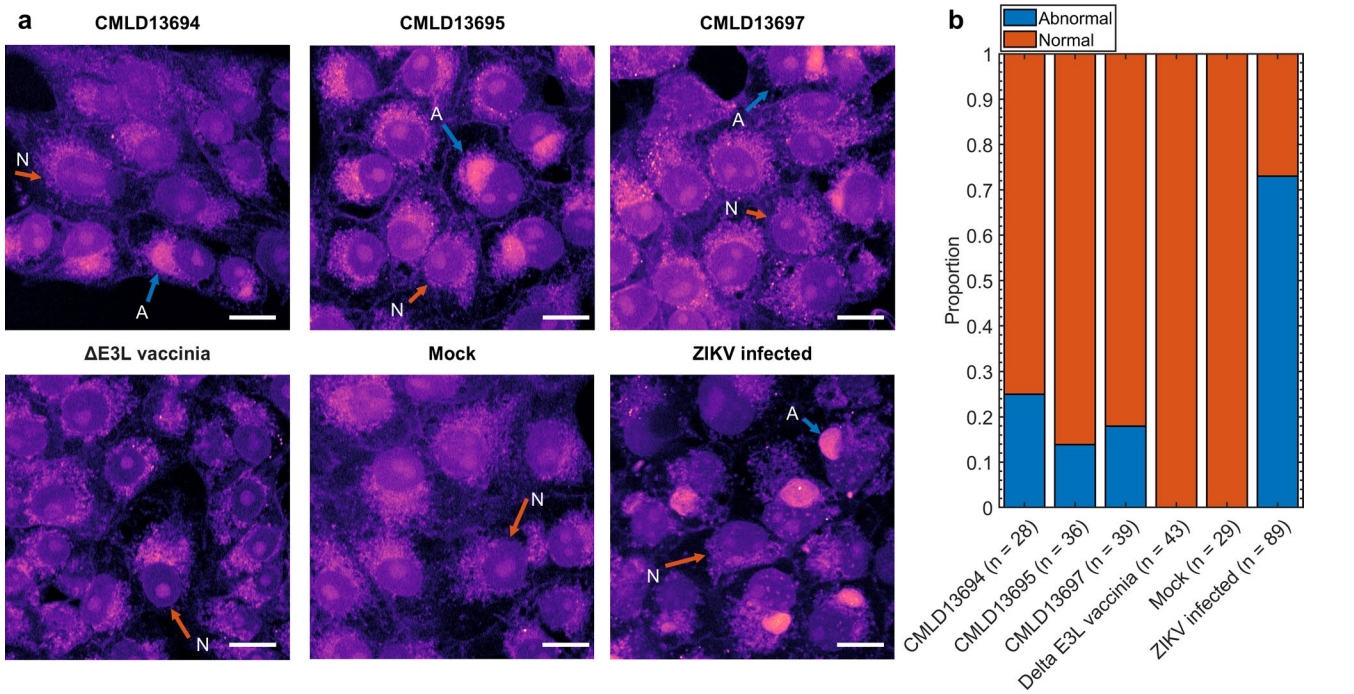

Extended Data Fig. 7 | Imaging virus infected cells after antiviral compounds treatment. (**a**) Example visible SRS images (at 2930 cm^{-1}) of antiviral compounds treated (CMLD13694, CMLD13695, CMLD13697, and ΔE3L vaccinia), mock, and ZIKV-infected VERO cells. Arrows with 'A' and 'N' indicate example abnormal and normal cells, respectively. 3 independent experiments were repeated with similar results. (**b**) Stacked bar plots of the proportions of the abnormal and normal cells in each group. Scale bars, 10 μm.

https://doi.org/10.1038/s41592-024-02575-1

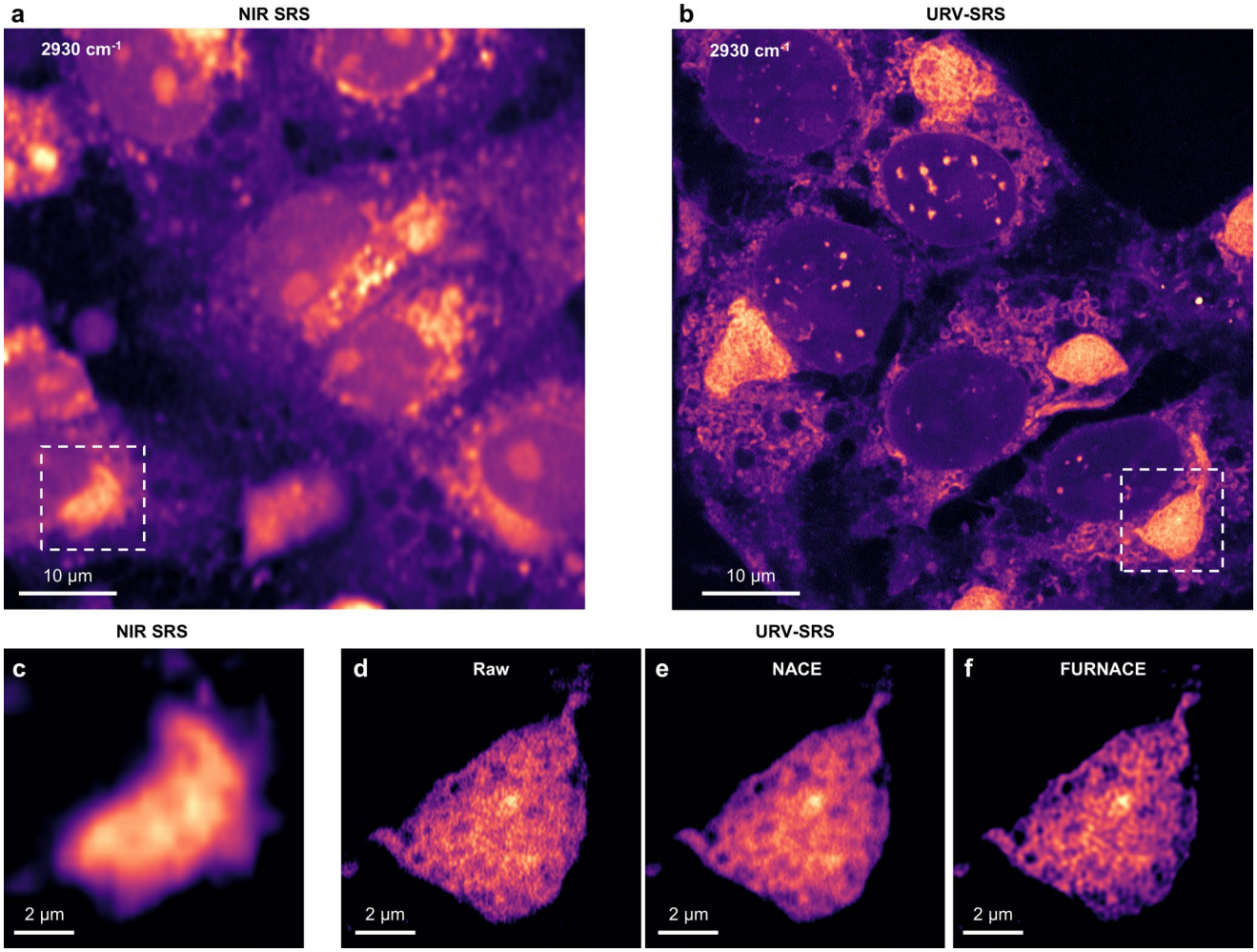

Extended Data Fig. 8 | Comparison between NIR SRS and URV-SRS imaging of virus replication sites. (**a**) NIR SRS imaging of ZIKV-infected cells at 2930 cm^{-1}. (**b**) URV-SRS imaging of ZIKV-infected cells at 2930 cm^{-1}. (**c**) Zoom- in of a replication site in the dashed box in (a). (**d**–**f**) Zoom-in of a replication site in the dashed box in (b). Raw visible SRS image, NACE denoising output, and FURANCE resolution enhanced output are sequentially shown from (d) to (f). 4 independent experiments were repeated with similar results.

https://doi.org/10.1038/s41592-024-02575-1

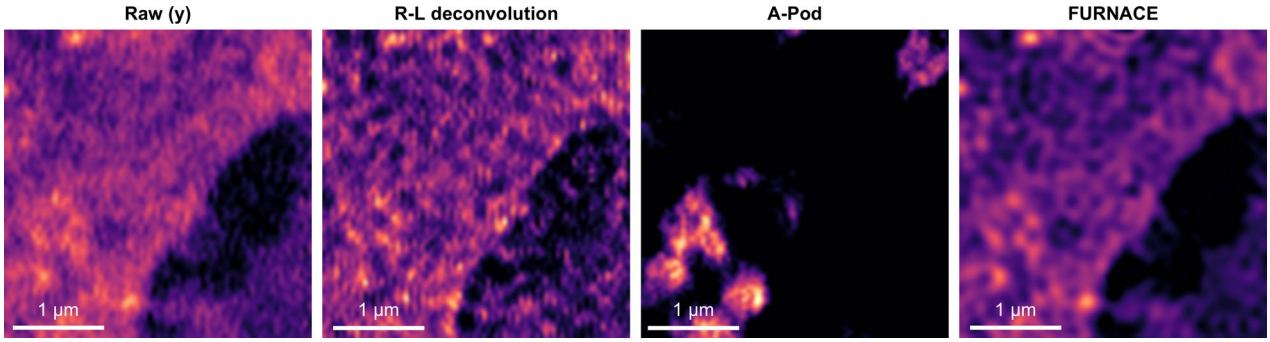

Extended Data Fig. 9 | Comparing FURNACE with other deconvolution methods. From left to right, Raw (y) SRS image, FURNACE output, Richardson-Lucy deconvolution (RL Deconv) output, and A-Pod output. 3 independent experiments were repeated with similar results.

https://doi.org/10.1038/s41592-024-02575-1

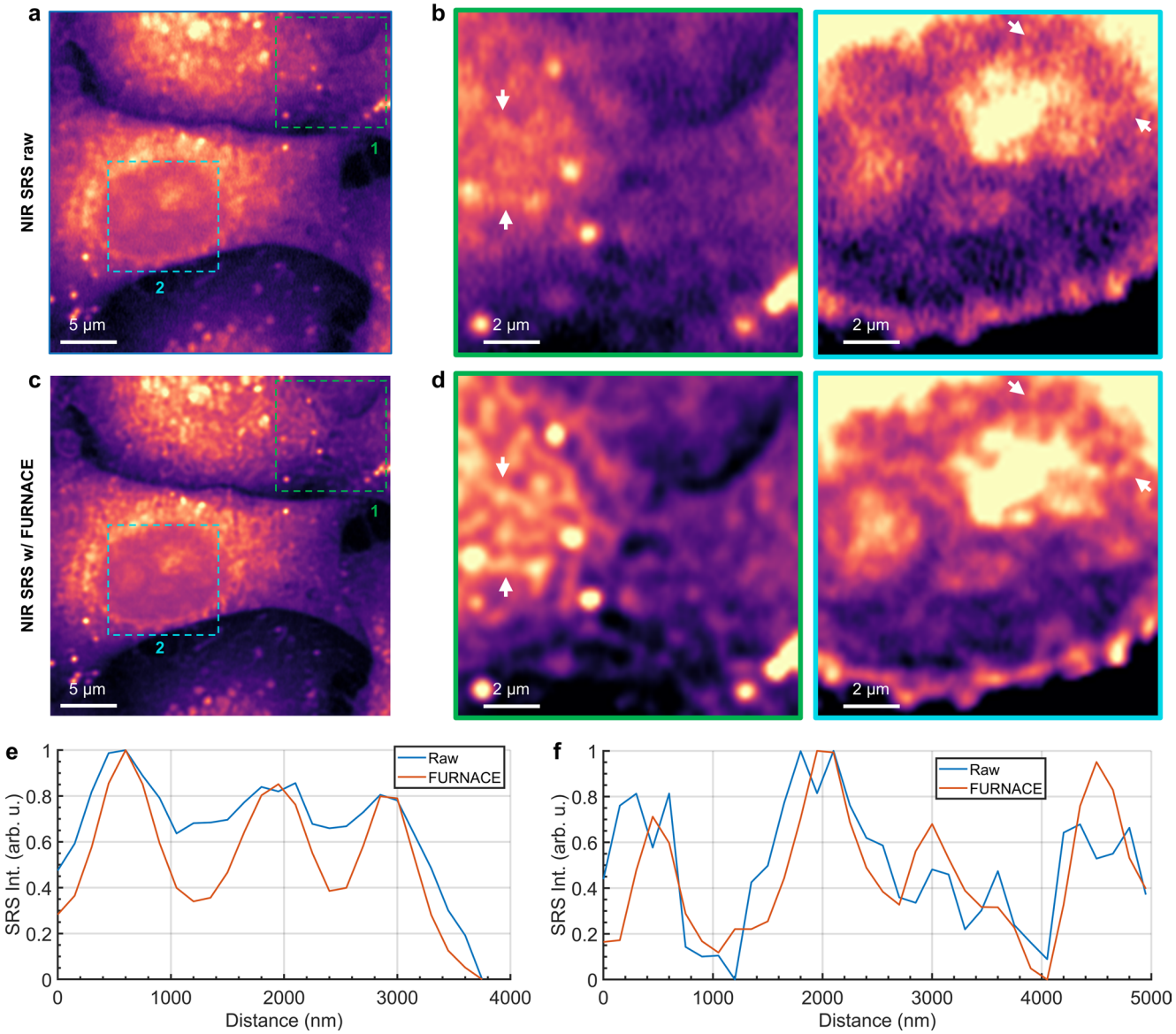

Extended Data Fig. 10 | Applying FURNACE to NIR SRS. (**a**) Raw NIR SRS imaging of mammalian cells at 2930 cm^{-1}. (**b**) Zoom-in of the cytoplasm (dashed box 1) and nucleus (dashed box 2) highlighted in (a). (**c**) The FURNACE output of the NIR SRS image in (a). (**d**) Zoom in on the highlighted regions in (c). (**e**) Line profiles between the two arrows in the cytoplasm (dashed box 1 in (b) and (d)). (**f**) Line profiles between the two arrows in the nucleus (dashed box 2 in (b) and (d)). 5 independent experiments were repeated with similar results.

nature portfolio

Corresponding author(s): Ji-Xin Cheng

Last updated by author(s): Nov 9, 2024

Reporting Summary

Nature Portfolio wishes to improve the reproducibility of the work that we publish. This form provides structure for consistency and transparency in reporting. For further information on Nature Portfolio policies, see our Editorial Policies and the Editorial Policy Checklist.

Statistics

For all statistical analyses, confirm that the following items are present in the figure legend, table legend, main text, or Methods section.

n/a	Confirmed	
☐	☒	The exact sample size (*n*) for each experimental group/condition, given as a discrete number and unit of measurement
☐	☒	A statement on whether measurements were taken from distinct samples or whether the same sample was measured repeatedly
☒	☐	The statistical test(s) used AND whether they are one- or two-sided *Only common tests should be described solely by name; describe more complex techniques in the Methods section.*
☒	☐	A description of all covariates tested
☒	☐	A description of any assumptions or corrections, such as tests of normality and adjustment for multiple comparisons
☐	☒	A full description of the statistical parameters including central tendency (e.g. means) or other basic estimates (e.g. regression coefficient) AND variation (e.g. standard deviation) or associated estimates of uncertainty (e.g. confidence intervals)
☒	☐	For null hypothesis testing, the test statistic (e.g. *F*, *t*, *r*) with confidence intervals, effect sizes, degrees of freedom and *P* value noted *Give P values as exact values whenever suitable.*
☒	☐	For Bayesian analysis, information on the choice of priors and Markov chain Monte Carlo settings
☒	☐	For hierarchical and complex designs, identification of the appropriate level for tests and full reporting of outcomes
☐	☒	Estimates of effect sizes (e.g. Cohen's *d*, Pearson's *r*), indicating how they were calculated

Our web collection on statistics for biologists contains articles on many of the points above.

Software and code

Policy information about availability of computer code

Data collection	Data was collected with LabView.
Data analysis	Individual NAC U-net denoisers and consensus equilibrium prediction were implemented in Python with Tensorflow. LASSO hyperspectral image analysis was written in Matlab. All the home-built codes are available at https://github.com/buchenglab

For manuscripts utilizing custom algorithms or software that are central to the research but not yet described in published literature, software must be made available to editors and reviewers. We strongly encourage code deposition in a community repository (e.g. GitHub). See the Nature Portfolio guidelines for submitting code & software for further information.

Data

Policy information about availability of data

All manuscripts must include a data availability statement. This statement should provide the following information, where applicable:

- Accession codes, unique identifiers, or web links for publicly available datasets
- A description of any restrictions on data availability
- For clinical datasets or third party data, please ensure that the statement adheres to our policy

Example data sets for for FURNACE and spectral unmixing are available at https://github.com/buchenglab. Larger datasets are available at Figshare (https://doi.org/10.6084/m9.figshare.26970583.v1)

Human research participants

Policy information about studies involving human research participants and Sex and Gender in Research.

Reporting on sex and gender	N/A
Population characteristics	N/A
Recruitment	N/A
Ethics oversight	N/A

Note that full information on the approval of the study protocol must also be provided in the manuscript.

Field-specific reporting

Please select the one below that is the best fit for your research. If you are not sure, read the appropriate sections before making your selection.

☒ Life sciences ☐ Behavioural & social sciences ☐ Ecological, evolutionary & environmental sciences

For a reference copy of the document with all sections, see nature.com/documents/nr-reporting-summary-flat.pdf

Life sciences study design

All studies must disclose on these points even when the disclosure is negative.

Sample size	For each NACE denoising application, we acquired ~ 6 FOVs and used data augmentation (including rotating and flipping) to increase the effective training image sample size. The rationale for sufficient sample sizes is based on observing that the training loss curves do not plateau due to insufficient sample size.
Data exclusions	No data was excluded from analysis.
Replication	Data and code were available at https://github.com/buchenglab. The NACE denoiser can be trained from scratch using the provided data. The model was trained several times and the results were reproducible.
Randomization	The training set was randomly generated from the pool of the raw image sequences.
Blinding	Raw data was blinded into the training and testing groups for training NACE denoisers. The training and testing sets were allocated randomly. The testing set was not evaluated during model training.

Reporting for specific materials, systems and methods

We require information from authors about some types of materials, experimental systems and methods used in many studies. Here, indicate whether each material, system or method listed is relevant to your study. If you are not sure if a list item applies to your research, read the appropriate section before selecting a response.

Materials & experimental systems

n/a	Involved in the study
☒	☐ Antibodies
☐	☒ Eukaryotic cell lines
☒	☐ Palaeontology and archaeology
☒	☐ Animals and other organisms
☒	☐ Clinical data
☒	☐ Dual use research of concern

Methods

n/a	Involved in the study
☒	☐ ChIP-seq
☒	☐ Flow cytometry
☒	☐ MRI-based neuroimaging

Eukaryotic cell lines

Policy information about cell lines and Sex and Gender in Research

Cell line source(s)	SKOV3 (HTB-77), VERO (CRL-1586), and SJSA-1 cells (CRL-2098) from American Type Culture Collection (ATCC).

Authentication	None of the cell lines were used for authentication
Mycoplasma contamination	Mycoplasma contamination test were not tested after purchase.
Commonly misidentified lines (See ICLAC register)	None